Cosmic muon tomography of pure cesium iodide calorimeter crystals

E. Frlež[a,1], I. Supek[b], K. A. Assamagan[a,c], Ch. Brönnimann[d,e], Th. Flügel[d,e], B. Krause[d], D. W. Lawrence[f] D. Mzavia[g], D. Počanić[a], D. Renker[d], S. Ritt[a], P. L. Slocum[a], N. Soić[b,e],

[a]*Physics Department, University of Virginia, Charlottesville, VA 22901, USA*

[b]*Institute Rudjer Bošković, Bijenička 46, HR-10000 Zagreb, Croatia*

[c]*Physics Department, Hampton University, Hampton, VA 23668, USA*

[d]*Paul Scherrer Institute, Villigen, CH-5232, Switzerland*

[e]*Physik-Institut der Universität Zürich, CH-8057 Zürich, Switzerland*

[f]*Arizona State University, Tempe, AZ 85281, USA*

[g]*Institute for High Energy Physics, Tbilisi State University, Tbilisi, Georgia*

Abstract

Scintillation properties of pure CsI crystals to be used in the shower calorimeter being built for precise determination of the $\pi^+\to\pi^0 e^+\nu_e$ decay rate are reported. Seventy-four individual crystals, polished and wrapped in a teflon foil, were examined in the multiwire drift chamber system specially designed for transmission cosmic muon tomography. Critical elements of the apparatus and reconstruction algorithms enabling measurement of spatial detector optical nonuniformities are described. Results are compared with a Monte Carlo simulation of an ideal detector light response. The deduced optical nonuniformity contributions to the FWHM energy resolution of the PIBETA CsI calorimeter for the $\pi^+\to e^+\nu$ 69.8 MeV positrons and the monoenergetic 70.8 MeV photons were 2.7% and 3.7%, respectively. The upper limit of optical nonuniformity correction to the 69.8 MeV positron low-energy tail between 5 and 55 MeV was +0.2%, as opposed to the +0.3% tail contribution for the photon of the equivalent total energy. Imposing the 5 MeV calorimeter veto cut to suppress the electromagnetic losses, `GEANT`-evaluated positron and photon lineshape tail fractions summed over all above-threshold ADCs were found to be 2.36±0.05(stat)±0.20(sys)% and 4.68±0.07(stat)±0.20(sys)%, respectively.

PACS Numbers: 87.59.F, 29.40.Mc, 24.10.Lx

Keywords: Transmission cosmic muon tomography; Scintillator light output and light collection probability; Scintillation detector pulse-height resolution

1 Introduction

The PIBETA collaboration has proposed an experimental program [1] with the aim of making a precise determination of the $\pi^+ \to \pi^0 e^+ \nu_e$ decay rate at the Paul Scherrer Institute (PSI). The proposed technique is designed to achieve an overall level of accuracy in the range of $\sim$0.5%, improving the present 4% branching ratio uncertainty [2]. The $(1.025 \pm 0.034) \times 10^{-8}$ pion beta ($\pi\beta$) decay branching ratio will be remeasured relative to the 10^4 times more probable $\pi^+ \to e^+ \nu_e$ decay rate, that is known with the combined statistical and systematic uncertainty of 0.4% [3,4].

The Standard Model description of the $\pi\beta$ decay and its radiative corrections [5] enables a stringent test of the conserved vector current (CVC) hypothesis and the unitarity of the Cabbibo-Kobayashi-Maskawa (CKM) quark mixing matrix. The most accurate extraction of the CKM matrix element V_{ud}, based on the superallowed Fermi transitions in nuclei, involves the theoretical nuclear overlap corrections that dominate the total 0.3% uncertainty [6]. The recent measurements of nine different nuclear transition rates confirm the CVC hypothesis at the level of 4×10^{-4}, but violate the three-generation CKM unitarity condition by more than twice the estimated error [7]. The complementary neutron decay experiments yield the result that also differs from unitarity by two standard deviations, but in the opposite sense [7]. It is of fundamental interest to measure the branching ratio of the $\pi^+ \to \pi^0 e^+ \nu_e$ process at the 0.5% level or better to check the consistency with the nuclear and neutron β decay values and the unitary prediction of the Minimal Standard Model (MSM). Moreover, the precisely measured $\pi\beta$ branching ratio could be used to constrain masses and couplings of additional neutral gauge bosons in grand unified theories. If such couplings are directly discovered at future collider experiments, precision low-energy data will be the essential ingredient in extending the MSM framework [8].

The central part of the PIBETA detector system is a high-resolution, highly segmented fast shower calorimeter surrounding the active stopping target in a near-spherical geometry. The requirements imposed on the calorimeter design were:

- high energy resolution for effective suppression of background processes,
- high segmentation and fast timing response to handle the high event rates,
- acceptable radiation, mechanical and chemical resistance, and
- compact geometry to simplify the operation and reduce the cost.

These design constraints are met in a spherical detector with individual calo-

[1] Corresponding author; Tel: +1–804–924–6786, FAX: +1–804–924–4576, e–mail: frlez@virginia. edu

rimeter modules made from undoped Cesium Iodide (CsI) crystals. The nonactivated alkali iodides have been known for more than thirty years to exhibit a near ultraviolet emission component when excited by ionizing radiation [9,10]. The pure CsI material was reintroduced as a fast, rugged, and relatively inexpensive scintillator material by Kobayashi *et al.* [11] and Kubota *et at.* [12,13]. The scintillation characteristics of pure CsI have been reported subsequently by a number of experimental groups. These investigations have covered the light readout techniques, scintillation decay times, origins of different emission components, crystal light yields, and energy and timing resolutions [14–19], radiation resistances [20,21], wrapping and tuning methods and the uniformity of light responses [24,25]. The design and/or performance of pure CsI electromagnetic calorimeters have been recently described in Refs. [26] (NMS at LAMPF/BNL), [27,28] (KTEV at FERMILAB), and [29] (PHENIX at RHIC).

The PIBETA calorimeter geometry shown in Fig. 1 is obtained by the class II geodesic triangulation of an icosahedron [30]. Selected geodesic breakdown results in 220 truncated hexagonal, pentagonal and trapezial pyramids covering the total solid angle of $0.77\times 4\pi$ sr. Additional 20 crystals cover two detector hemispheres open to the beam and act as shower leakage vetoes. The inner radius of the crystal ball is 26 cm, and the axial module length is 22 cm, corresponding to 12 CsI radiation lengths (X_0=1.85 cm [31]). There are nine different module shapes: four irregular hexagonal truncated pyramids (we label them HEX–A, HEX–B, HEX–C, and HEX–D), three regular pentagonal (PENT) and irregular half-hexagonal truncated pyramids (HEX–D1 and HEX–D2), and two trapezohedrons which function as vetoes (VET–1, VET–2). The volumes of our CsI crystals vary from 797 cm^3 (HEX–D1/2) to 1718 cm^3 (HEX–C).

All key components of the complete PIBETA detector have been prototyped and/or built and have met the required specifications [32]. All the detector components were delivered to PSI by mid-1998. The final assembly of the apparatus was followed by the in-beam commissioning and calibration. "Production" measurements should begin in 1999, and will extend over two more years to complete the first phase of the project, a $\sim$0.5% measurement of the $\pi^+\to\pi^0 e^+\nu$ decay rate.

The quality of the delivered CsI calorimeter crystals was controlled in the following program of measurements:

- check precisely the crystal mechanical dimensions against the specifications,
- study the effects of different crystal surface treatments and wrapping configurations on the energy and timing resolution and on the uniformity of light response,
- determine the percentage of a fast scintillation component in the light out-

put,
- measure the contribution of detector photoelectron statistics to energy resolution,
- find the temperature dependence of a detector ADC readings, and
- determine axial and transverse optical nonuniformities for each crystal.

The ultimate goal of the program was to provide the input parameters for the Monte Carlo simulation of the calorimeter response and deduce the effects of CsI crystal light yields and optical nonuniformities on the energy lineshapes of the 10–120 MeV photons and positrons.

The cosmic muon spectra have been used to examine the uniformity of light response of two large (24×36 cm) cylindrical NaI(Tl) calorimeter crystals in the earlier work of Dowell *et al.* [33]. Their apparatus relied on the plastic scintillator hodoscopes with the 3.8×3.8 cm^2 cross section for the charged particle tracking. The precision of the trajectory reconstruction was therefore limited to $\sim$4 cm. Such positional resolution was deemed inadequate for our application because the PIBETA CsI crystals have an axial length of 22 cm with front (back) surface side lengths of less than 4 cm (7 cm).

Most of our measurements were done with the tomography apparatus built around three pairs of multiwire drift chambers (MWDC) using the cosmic muons as a probe. One dozen of PIBETA CsI detectors were examined in a 350 MeV/c minimum ionizing muon beam of the PSI πE1 area, as well as in the 405 MeV/c penetrating pion and stopping proton beams in the πM1 channel. Selected CsI crystals were also scanned with a 662 keV ^{137}Cs γ-source. The light yield nonuniformities measured in the beam and with a radioactive-source scan method were compared with more precise cosmic muon tomography data. The experimental apparatus used for a γ-source crystal scans and the subsequent data reduction were simple enough to be easily adopted by the crystal manufacturers, thus accelerating the quality control cycle in the future.

2 Crystal Production, Mechanical Quality Control and Surface Treatment

Pure CsI crystals produced for the PIBETA calorimeter came from two different sources. Twenty-five crystals were grown and cut to specified shapes in the Bicron Corporation facility in Newbury, Ohio. The rest of the scintillators were grown in the Institute for Single Crystals in Kharkov, Ukraine. Preliminary examination of fifty-five Kharkov CsI crystals, including the mechanical and physical tests, was done in the High Energy Institute of Tbilisi University, Georgia.

Manufacturing tolerances of the crystals were specified for the linear dimensions (+150 μm/−50 μm) and for the angular deviations (+0.040°/−0.013°). Geometrical dimensions of the machined crystals were confirmed at PSI using the computer-controlled distance-measuring device *WENZEL Precision*. The machine was programmed to automatically probe the surfaces of a crystal with a predefined shape. Each crystal surface was scanned with a touch head at six points and the equations of planes were found through these surveyed points. Body vertices, measured with an absolute precision of 2 μm and reproducible within 20 μm, were then compared with the expected theoretical values. Those crystals that failed the imposed geometrical tolerances were returned to a manufacturer for reuse as a raw crystal growing material.

The crystal surfaces were polished with a mixture of 0.2 μm aluminum oxide powder and etylenglycol. The light output of the fast CsI scintillation component (F) that is completely decaying in first 100 ns, relative to the total CsI signal (T), integrated in 1 μs gate, was measured next. These measurements were done with the unwrapped crystals using air-gap coupled photomultiplier tubes (PMTs) and a Tektronix TDS 744 digital oscilloscope. Only the crystals with a fast-to-total component ratio (F/T) better than 0.7 were accepted. The mean value of fast-to-total ratio for all accepted CsI crystals was 0.788, see Fig. 2.

Three inch EMI photomultiplier tubes 9821QKB [35] were glued to the back faces of hexagonal and pentagonal CsI crystals using a 300 μm layer of silicone Sylgard 184 elastomer (Dow Corning RTV silicon rubber plus catalyst). Smaller half-hexagonal and trapezial detector modules were equipped with two inch EMI 9211QKA phototubes [35]. The resulting crystal–photomultiplier tube couplings were strong and permanent, but could be broken by application of a substantial tangential force. The PMT quartz window transparency, peaking at ∼380 nm [35], is approximately matched to the spectral excitation of a pure CsI fast scintillation light component with a maximum room temperature emission at ∼310 nm [15]. The PMT high voltage dividers were modified EMI-recommended bases designed and built at the University of Virginia. These dividers minimized the so-called "super"-linearity exhibited by many PMTs well below the onset of saturation. The maximum PMT nonlinearity measured with a pair of light-emitting diodes was less than 2% over the full dynamic range expected in the $\pi\beta$ decay rate measurement [36].

Four different wrapping materials for lateral crystal surfaces were investigated in wrapping and tuning studies with 405 MeV/c pion and proton beams in PSI μM1 area:

- one to five layers of a 38 μm PTFE Teflon sheet (CF_2 monomer, X_0=16.0 cm),
- one to five layers of 30 μm Mylar sheet ($C_5H_4O_2$, X_0=28.7 cm),

- a 250 μm thick Tyvec fleece (polyethylene CH_2, X_0=131.3 cm), and
- a 110 μm thick Millipore filter (polyvinylidene fluoride PVDP, X_0=19.0 cm) with 0.22 μm pores.

In all cases a primary diffuse reflector was protected by an additional 20 μm thick aluminized Mylar cover. These preliminary tests showed more uniform axial light collection from the crystal front section when a polished front crystal surface was covered by a black paper sheet. A similar tuning method, using black paper strips at the front section of $5\times6\times36$ cm^3 CsI(Tl) crystals in order to improve the uniformity of light collection, was recently described in Ref. [25].

The maximum fast-to-total ratio was always achieved with unwrapped crystals because all applied wrapping materials absorb more ultraviolet light which dominates the fast component, than visible light. A two-layered teflon cover was found to be superior in delivering $\geq$20% more fast scintillation light component than the other reflectors. It was also comparatively better in not degrading the F/T ratio by more than $\sim$2%. These differences in measured light output were reproducible in the beam tests with $\sim$1% event statistics and estimated 2% systematic uncertainty. They are subsequently confirmed in more controlled cosmic muon tomography measurements.

On the basis of these findings the standard wrapping configuration for all studied CsI crystals consisted of the lateral surfaces being wrapped with two layers of Teflon foil plus one layer of aluminized Mylar sheet, and the front crystal surface covered with the black paper template. The back crystal surface with the glued phototube was left uncovered.

Light yield measurements were repeated for a subset of crystals after six months period to confirm that no appreciable changes occurred as a result of degradation of the surface reflectivities and wrapper material qualities. The light outputs were typically within 5% of previously measured values.

The alternative surface treatment of CsI crystals, involving the painting of lateral crystal surfaces with the patented waveshift lacquer, was recently studied by our group in a large sample of CsI detectors. The light response and uniformity properties were noticeably improved, resulting in the better energy resolutions for the 70 MeV monoenergetic e$^{\pm}$ and 50–82 MeV tagged photons. The possible degradation and change in the crystal surface reflectivities that could be difficult to account for in the multi-year long precision experiment like the PIBETA is also expected to be arrested by such a treatment. These measurements will be covered in detail in the forthcoming paper [37].

3 Tomographic Apparatus

The simplified layout of the tomographic apparatus is illustrated in the GEANT rendering showing a few simulated cosmic muon trajectories on Fig. 3. Three identical delay-line readout drift chambers are used to define the cosmic muon tracks intersecting CsI crystals. The chambers were built at Los Alamos Meson Physics Facility (LAMPF) by the M. Sadler group from Abilene Christian University. This type of drift chambers has been used reliably for years with the LAMPF spectrometers [38–41]. Each chamber consists of two signal and three ground planes with the nominal active area of 60×60 cm^2. The horizontally oriented "x" and "y" signal planes are two orthogonal sets of alternating cathode and anode wires evenly spaced at 0.4064 cm.

The light-tight aluminum box had two chamber pairs mounted on its top plate, and one pair fixed below the bottom side. Distances between the chamber pairs 1–3 and 2–3 were 24 cm and 27 cm, respectively. The dark box could accommodate up to six CsI calorimeter modules at one time. It had feedthrough connectors for twelve signal and twelve high voltage cables as well as six temperature sensor lines and six calibration LED signal cables. A pair of 1 cm thick plastic scintillators were placed directly below the apparatus and separated from the chamber system by a 5 cm layer of lead bricks shielding out the soft cosmic ray component. The Monte Carlo simulation (see Sec. 8.1) showed that hard cosmic muons penetrating the frames of the apparatus, CsI crystals and shielding material while triggering two scintillators had a smooth energy threshold starting at $\sim$120 MeV. The zenithal angle range of accepted cosmic muon trajectories intersecting all three MWDCs and at least one CsI detector was $\pm45^\circ$.

The chambers were operated with anode wires held at positive voltage between 2400–2600 V. The chamber cathode wires were grounded. The gas mixture was 65% argon, 35% isobutane and 0.1% isopropyl alcohol. Detection efficiencies of individual chambers for penetrating cosmic muons exceeded 90%, with the combined six-chamber efficiency routinely surpassing 50%.

Anode wires were attached directly to a 2.5 ns/cm fast delay-line. Signals from both ends of the delay line were amplified twenty-fold, discriminated at a 10 mV threshold and connected to two channels of a time-to-digital converter (TDC, LCR 2229A). The time difference in the two TDC readings identified the fired anode wire. Cathode lines defining the alternate field [42,43] were connected to one "odd" (O) and one "even" (E) line, and the signals on these lines were processed by a custom-made electronics unit which added and subtracted the analog pulses [44]. The electronic sum of cathode pulses (O+E) was discriminated and the resulting delayed signal determined the drift position timing, and was used to stop another TDC channel. The difference of the cathode signals (O$-$E) was digitized with an analog-to-digital converter (ADC, LCR 2249A). That information was used to discriminate between the events that make the ionization tracks left and right of the given anode wire. The 100 ns integration gate timing was defined by a (O+E) logic pulse timing. Four measurements were therefore required to find an intersection between a cosmic muon track and one drift chamber plane, namely three TDC values and one ADC value. The schematic diagram of the electronic logic is shown in Fig. 4.

Advantages of the system were good charged particle track resolution ($\sim$0.5 mm root-mean-square in the horizontal plane, Fig. 5), stability to fluctuations in the outside environmental parameters (humidity, temperature and pressure) and low cost of the associated electronics logic and readout. Limited counting rate and restriction to single hit events in the chambers did not represent a drawback in this tomographic application. The apparatus was operated in an air-conditioned room with the controlled humidity level kept below 30%. The temperature at six points inside the dark box as well as absolute time were recorded for every triggered event. The temperature range recorded inside the dark box during three years of data taking was ($22^\circ \pm 3^\circ$)C. The typical temperature gradient was 0.4°C/day, leading to average 0.2°C absolute temperature variation and $\sim$0.4% average CsI ADC scale change in a single data taking run (fixed at 250000 triggers, $\sim$6 hours). Measured light output variations of the CsI crystals and the PMT gain drifts caused by daily temperature cycles were corrected for in the replay analysis (see Sec. 6).

4 Data Acquisition System

The computer code used for data acquisition was HIX (Heterogeneous Information Exchange), a data acquisition system developed by S. Ritt at PSI, originally intended for use in small and medium-size nuclear physics experiments [45].

The 486 personal computer called "frontend" was connected to a CAMAC crate via a HYTEC 1331 interface that read ADC, TDC, scalar, and temperature sensor units. The C program running under MS-DOS accessed data and sent it over the network to a VAX 3100 server. A simple communication program on a VAXstation received data from the frontend computer and stored it in a global section buffer. Buffered data were passed by the Logger application to a user-written Analyzer program. Analyzed events were subject to predefined cuts, filled in predefined histograms, and stored in a raw data stream directed simultaneously to a hard disk drive and a 8-mm tape system. The experiment was controlled from a PC computer by a Microsoft Windows control program. A windows-based graphical user interface to the program allowed starting, pausing and stopping data acquisition, as well as an online inspection of individual raw data words, calculated data words, scalars, assorted efficiencies, one and two-dimensional histograms, and gate, box and Boolean tests. Different PC computers on the Ethernet could make a connection to the VAX server called Link and access the same information remotely.

In data acquisition mode only the events for which at least two x and two y drift chambers had nonzero ADC and TDC values were written to an disk-resident ASCII Data Summary File (DSF). One accepted event contained 55 raw data words specifying the response of the MWDCs and CsI detectors, instantaneous temperatures and absolute times. That was a set of events for which a cosmic muon trajectory could be unambiguously reconstructed. A raw trigger rate was $\sim$13 Hz with six CsI crystals in the dark box. The average DSF event rate was $\sim$4 Hz. Individual runs were stopped and restarted automatically after 250000 collected triggers. A total of about 10^5 DSF events per crystal were typically collected in one week of data acquisition. Tomography data for one set of six crystals were usually collected over a two week period.

5 Drift Chamber Calibration

Two different trigger configurations were used interchangeably during the data collection. Drift chamber calibration was done with a trigger requiring a two-scintillator coincidence and good ADC and TDC data for at least one drift chamber. In the tomography data acquisition mode, the triple coincidence between two tag scintillators and one CsI detector was required, accompanied by at least one good pair of x and y chamber hits. The rare accidental coincidences involving signals in more than one CsI detector were eliminated from the DSF records in the offline analysis.

The hit anode wire number n_A was calculated from

$$n_A = \frac{(T_1 - T_2 + N \cdot D)}{2D}, \quad (1)$$

where T_1 and T_2 were the TDC values for two ends of the anode delay line, N was the number of wires in a chamber (between 71 and 73), and D was the $\sim$2.05 ns time delay between the adjacent wires. Truncated wire position x_T was defined as the nearest integer multiple n_A of the 0.8128 cm wire separation g:

$$x_T = \mathtt{NINT}(n_A \cdot g). \quad (2)$$

The anode delay time difference $(T_1 - T_2)$ depended nonlinearly on the anode position. Linearized anode wire positions for each chamber were approximated by a polynomial expansion

$$x_A = \sum_{i=0}^{m} c_i \cdot (T_1 - T_2)^i, \tag{3}$$

where the order m of the fit with the chi-square per degree of freedom $\chi^2/(m-1)\approx 1$ depended on the particular delay line. For our chambers the orders of the fits were 3, 4, or 5. The coefficients c_i were optimized with a `MINUIT` program [46] that minimized the sum of squared deviations $(x_T - x_A)^2$ for each chamber in every run.

The drift distance d_x was determined from the drift timing T_x using the calibration lookup table $f(T_x)$

$$d_x = f(T_x) \cdot T_x + \Delta T_x, \tag{4}$$

where ΔT_x was the drift time offset. The lookup table was calculated assuming that incoming cosmic muons are distributed uniformly over the equidistantly spaced wires.

The final hit position x was given by expression:

$$x = x_T + (-1)^n \cdot \texttt{SIGN}(\mathrm{ADC_{O-E}} + \mathrm{ADC_0}) \cdot d_x + x_{\mathrm{OFF}}, \tag{5}$$

where x_{OFF} was the chamber x coordinate offset, and $\mathrm{ADC_{O-E}}$ and $\mathrm{ADC_0}$ were the (O−E) ADC signal and associated offset, respectively.

The individual chamber phases n in the Eq. (5) and absolute horizontal coordinate offsets between six chambers were adjusted with help of two-dimensional histograms $(x_1 - x_3)$ vs $(x_2 - x_3)$ and $(y_1 - y_3)$ vs $(y_2 - y_3)$ [47,48].

6 Raw Data Reduction

Data summary files are analyzed offline by compressing the DSF event data into `PAW` Ntuples [50]. Drift time-to-distance lookup tables and assorted chamber calibration constants, as well as CsI detector ADC pedestals and ADC temperature corrections, were determined for each run separately. The high voltages of the CsI detector phototubes were selected to give ~8 ADC channels/MeV scale. The FWHMs of the pedestal peaks were typically 2 ADC channels. Therefore, the pedestal width contribution corresponded to an energy deposition of 0.25 MeV, 24 μm pathlength or 0.5% of the most probable energy deposition by a minimum ionizing charged particle. Drifts in the pedestal position over a one month period amounted to less than 2 ADC channels.

The precise horizontal coordinate offsets of six CsI crystals inside the dark box were determined in the next stage of analysis. Using the preliminary offsets read from the plastic template, between 5 and 10 percent of the reconstructed cosmic muon trajectories were found not to intersect any of the predefined detector volumes. After adjusting the x and y translation software offsets of CsI modules by maximizing the number of tracks intersecting crystal volumes, the real number of events undergoing scattering in the apparatus or having the improperly reconstructed tracks was shown to be below 1%. That percentage is in agreement with the Monte Carlo simulation of cosmic muons interacting with the experimental apparatus, showing the most probable muon scattering angle of 0.25° and the 2.5° mean scattering angle. The Monte Carlo mean-square-root of the scattering angle for the accepted events was 0.66°. That value translates into an average pathlength uncertainty of 1 mm. The estimated error in finding the correct crystal position inside the dark box was smaller than $\sim$0.5 mm, Fig. 6.

The energy deposited in CsI crystal by cosmic muons along the fixed pathlength is a broadened distribution due to the statistical nature of energy transfers. Maximal measured pathlengths were up to 12 cm, while the average pathlength was $\sim$6 cm. A Gaussian model for the energy loss distribution of the minimum ionizing particles in the CsI thicknesses less than 12 cm is not a good approximation. The distribution of energy losses is asymmetric one, with a long high energy tail: the most probable energy loss is smaller than mean energy loss [51].

The light yield temperature coefficients for the individual CsI detectors were determined by the "robust" estimation [52] of the ADC values per unit pathlength as a linear function of temperature recorded inside the dark box. The least-squares condition assumes the normally distributed measurements with constant standard deviations and is therefore not appropriate in this application, as pointed out above. Typically, more than 10^5 cosmic muon events, collected over at least one week and spanning the temperature range of $\sim$2°C, were used as an input experimental data set. The `FORTRAN` subroutine `MEDFIT`, documented in the Ref. [53], was adopted as a fitting procedure by imposing the requirement of the minimum absolute deviation between the measured and calculated ADC values per unit path that were dependent linearly on the temperature variable. The average light output temperature coefficient for 74 different CsI detectors extracted by that method was $-1.4\%/°\mathrm{C}$, both for fast and total scintillation light components. These numbers are in an agreement with the previously reported value of $-1.5\%/^\circ$C [11], but the spread of extracted coefficients for different CsI detectors was large: $\pm 4\%/^\circ$C. We point out that the method did not allow us to separate the temperature dependence of the light outputs from the temperature instabilities of the phototubes and high voltage dividers as well as the temperature instabilities of ADC modules itself. The LeCroy catalogue specification [54] lists the typical temperature coefficient of LCR 2249A ADC unit as zero, and the maximum coefficient up to $\pm 3\%$ for an ADC gate longer than 100 ns and an average ADC reading of 75 pC (about a quarter of a full 256 pC scale).

The raw ADC values were corrected for the temporal temperature variations and written into the revised DSF files used in subsequent analysis.

7 Detector Photoelectron Statistics

The contribution of the photoelectron statistics to the energy resolution of CsI crystals was determined by a photodiode-based system. Six individual detectors (CsI crystals with photomultiplier tubes and high voltage dividers) having identical photodiodes (LEDs) coupled to their back sides were placed inside the cosmic muon tomography apparatus. The LEDs were pulsed at a 10 Hz rate using a multichannel diode driver with a continuously adjustable output voltage. One split output signal from each channel of the driver generated a 100 ns wide ADC gate. The LED light in a CsI detector produced fast ($\sim$20 ns FWHM) PMT anode pulses whose integrated values depended on driving voltage and were equivalent to the fixed cosmic muon energy depositions between 10 and 100 MeV.

A total of five different LED amplitudes were used in measurements of each CsI detector. Examples of the LED spectra are shown in Fig. 8. The ADC pedestals were recorded simultaneously during the run. The intensity of LED light was cross-calibrated against the cosmic muon spectra peaks in CsI crystals. These muons were tracked in tomography drift chambers and both their pathlengths and energy depositions in the crystals could be easily calculated. That calculation enabled the establishment of the absolute energy scale in MeV.

The variance σ_E^2 of a photodiode peak depended upon the mean number of photoelectrons $\bar{N}_{pe}$ on the photocathode created per unit energy deposition in the crystal:

$$\sigma_E^2 = \sum_i \sigma_i^2 + \bar{E}/\bar{N}_{pe}, \tag{6}$$

where $\bar{E}$ was a LED spectrum peak position and σ_i^2's were assorted variances, such as instabilities of the LED driving voltage and temporal pedestal variations. Five measured points (σ_E^2,$\bar{E}$) were fitted with a linear function (6) and the mean number of photoelectrons per MeV for each CsI detector was determined. The statistical error of the least-squares fits was typically less than one photoelecton/MeV. Using the previously extracted light output temperature coefficients (Fig. 7) all $\bar{N}_{pe}$ values were scaled to the 18°C point. That value was the designed operating temperature of the PIBETA calorimeter.

The number of extracted photoelectrons per MeV for the fast scintillation component fell into the 20–130 range as shown on the Fig. 9. The hexagonal and pentagonal crystals equipped with three inch phototubes averaged 73 photoelectrons/MeV, while the half-hexagonal and veto detectors with two inch phototubes had a mean of 33 photoelectrons/MeV. The 73/33 ratio is almost perfectly explained by the $(3/2)^2$ ratio of photosensitive areas for two different photocathode sizes. The measured photoelectron statistics were in agreement with the 100 ns ADC gate values of $\bar{N}_{pe}$=(20–260) for large ($\sim$10 cm) pure CsI crystals equipped with two or three inch PMTs reported in the past in the Refs. [15–17,26].

The quantum efficiency of our bialkali photocathodes for pure CsI scintillation light is 23% [35], the average light collection probability for our detector shapes 23% (Sec. 8.2) and the fraction of deposited energy converted into the scintillation light was about 12%. Therefore, starting from the mean number of 73 photoelectrons/MeV we calculate that 1 MeV energy deposited in the CsI crystal produced on average 10^4 scintillation photons.

8 Monte Carlo Description

8.1 Tomography System

Geometrical layout of the experimental apparatus was defined using the `GEANT` detector description and simulation tools [49]. The active elements of the simulated apparatus were an aluminum box housing six CsI modules, six multiwire drift chambers, two scintillator planes and a layer of lead brick shielding, all shown in Fig. 3. Generated events were muons with the energy, angular and charge distribution of a hard cosmic ray component at sea level. The zenithal angle θ_z distribution of muons at the ground was assumed to be proportional to $\cos^2\theta_z$; the momentum spectrum between 0.1 and 10^3 GeV/c and the energy-dependent ratio of number of positive to number of negative cosmic muons was parameterized from the data given in Refs. [31,55].

A simulation trigger was defined by requiring a minimum energy deposition of more than 0.2 MeV in each scintillator plane. This threshold was about one-tenth of the minimum-ionizing peak in the triggered scintillator and corresponded to the discriminator level used in the data acquisition electronics.

Penetrating cosmic muons and generated secondary particles were tracked through the apparatus, and energy depositions, pathlengths in CsI crystals and hits in the drift chambers were digitized. All physical processes were turned on in the `GEANT` programs with the cutoff energies of 0.2 MeV for charged particles and photons. Inspection of simulated energy deposition spectra showed deviations from theoretical Vavilov distributions [51] expected in the planar detector geometries. The differences were caused by multiple scattering in the irregularly shaped crystals, and were particularly prominent for the events with shorter pathlengths close to the crystal edges. The simulated ADC histograms revealed that triggering cosmic muons deposit on average 10.33 MeV/cm in a CsI detector, with the most probable energy loss 5.92 MeV/cm.

Cosmic muon spectra in CsI detectors were described in a satisfactory way ($\chi^2/(m-1)\approx 1.2$) by the combination of a Gaussian distribution and a falling exponential tail:

$$\mathring{A}(\epsilon) = \theta(\epsilon_0 - \epsilon) e^{-\frac{1}{2}[(\epsilon-\bar{\epsilon})/\sigma_\epsilon]^2} + \theta(\epsilon - \epsilon_0) e^{\alpha - \beta\epsilon}, \tag{7}$$

where ϵ is energy (in MeV) deposited in one full CsI module. Parameters $\bar{\epsilon}$, σ_ϵ, ϵ_0, α, and β are extracted from the `GEANT` spectra by imposing the least squares constraint to the fit and leaving the pathlength d (cm) as free parameter:

$$\begin{aligned}
\bar{\epsilon}(d) &= 5.079 + 0.1876d - 9.9390 \cdot 10^{-3} d^2, && (8)\\
\sigma_\epsilon(d) &= 0.3545 + 7.2329 \cdot 10^{-3} d - 3.4148 \cdot 10^{-4} d^2, && (9)\\
\epsilon_0(d) &= 5.1800 + 0.1989d - 1.0297 \cdot 10^{-2} d^2, && (10)\\
\alpha(d) &= 4.0581 + 0.4465d - 1.5760 \cdot 10^{-2} d^2, && (11)\\
\beta(d) &= 0.7952 + 5.0313 \cdot 10^{-1} d - 1.5240 \cdot 10^{-3} d^2, && (12)
\end{aligned}$$

and

$$\theta(\epsilon_0 - \epsilon) = \begin{cases} 0, & \text{if } \epsilon_0 < 0, \\ 1, & \text{otherwise.} \end{cases} \tag{13}$$

These Monte Carlo spectra, broadened with the photoelectron statistics, could be used to describe our cosmic muon lineshapes produced by the optically uniform CsI detectors.

8.2 Light Collection Simulation: `TkOptics` *Code*

Propagation of scintillating photons through a uniform detector with the ideal reflecting dielectric surfaces and different wrapping materials was studied using the `TkOptics` simulation program [56,57]. The code is a library of `FORTRAN` subroutines with an X-Windows-based user interface written with `Tck/Tk` toolkit [58]. The program can simulate the light output response of an arbitrary shaped scintillation detector with given bulk and surface optical properties.

The polygonal detector shape is defined by the coordinates of its vertices. The detector attributes are reflector types of lateral and front crystal surfaces and wrapper material, crystal surface-wrapper gap distances and characteristics of a photomultiplier tube and a phototube-crystal joint coupling. The program handles normal dielectric, specular, diffuse and partially absorbent reflector surfaces with the arbitrary diffuse fraction, roughness, and specular r_s and diffuse reflectivity r_d. Predefined bulk properties of a detector are the medium scattering and attenuation length as well as refractive index. A photomultiplier tube is specified by the diameter, position and quantum efficiency of the photocathode.

Different choices of initial scintillating photon distribution are possible, the default being a uniform starting distribution throughout the scintillating volume. A working volume is a box divided into elementary cubic cells of fixed size. Output menu options include the initial and endpoint photon coordinates, and direction vectors and timing distributions of the detected scintillation photons organized in a `PAW` Ntuple. Every elementary cell is flagged as a bulk or edge crystal cell. Center coordinates of the cells and a fraction of photons generated in every cell, and subsequently detected on the PMT sensitive surface, are always recorded. Results of high statistics runs with 10^7 photons generated uniformly through the detector volume were plotted to show the number of photoelectrons generated as a function of scintillation source position inside the crystal. The relative statistical errors of calculated light collection probabilities for the bulk crystal cells were $\leq$2%.

The bulk attenuation length and the light scattering length of the near-ultraviolet emission component inside the CsI crystals was set to 150 cm and 200 cm, respectively [59]. The index of refraction for CsI medium increases from 1.82 for the blue-green light to about 2.08 for the ultraviolet light [59].

The simulated light collection probabilities $P(x, z)$ that depend on axial z and transverse x positions are shown integrated in the vertical y dimension in form of the lego plots for one wrapping configuration and two different crystal shapes in Figs. 10 and 11. The coordinate system is defined with the z=0 cm origin at the front face of the crystal and a photocathode window at z=22 cm plane.

We find that simulated light response of the ideal hexagonal or pentagonal PIBETA CsI detector with the specular lateral surfaces and a diffuse wrapping material can be described with:

- the average photon collection probability P for a three inch photocathode is about 23% for ideal r_s=1.0 crystal surfaces and a r_d=0.9 diffuse wrapper, decreasing by half, to 12% for r_s= 0.8,
- the axial light collection probability variation through the first 10 centimeters is in the $\pm$5% range, with a positive slope for higher specular and diffuse reflectivities, namely for $r_{s,d}\geq$0.9,
- the axial detected light variation in the back crystal half ($z\geq$10 cm) is up to $-$30%,
- the transverse light response referenced to the light yield at the crystal axis typically increases towards the crystal surfaces by up to +5% for $z\leq$10 cm, but is generally declining away from the central axis by $-$30% at the z=18 cm plane,
- the root-mean-square of a three-dimensional light nonuniformity is between 2.5% and 3.5% for $z\leq$10 cm, compared to a $\sim$20% root-mean-square for a $z\geq$ 10 cm volume, where a large spread is caused by the inefficient light collection from crystal back corners.

For lateral surfaces painted with a $r_d\approx$0.9 diffuse substance without an air gap we find that the average photon collection probability is lower, $\sim$17%, and the axial light collection nonuniformity as a function of axial position is always positive and is usually larger than +10% in a 22 cm long detector, making the root-mean-square of the 3D nonuniformity function $\geq$20%.

The Monte Carlo results for the optically uniform half-hexagonal and trapezial CsI crystals with the same range of optical properties predict smaller light yields and somewhat higher light collection nonuniformities:

- the average photon collection probability with a two inch photocathode is about 12%,
- the typical axial nonuniformity is positive in front, +5%/10 cm, and negative in the back crystal half, with a $-$30%/10 cm variation,
- the simulated transverse light output from the front crystal half is very similar to one for the full crystal shapes, increasing up to +3% away from the detector central axis, but decreasing by almost a third in the back corners of the crystal,
- the root-mean-square of detected light output varying between 3.0% and 4.5%, in the front ($z\leq$10 cm) and back ($z\geq$10 cm) crystal halves, respectively.

These light collection probability distributions calculated for optically homogeneous crystals explain the major features of measured optical nonuniformities presented in the next sections.

9 Measured Nonuniformities of CsI Detector Light Responses

The three-dimensional light output of the scintillation detector can be specified by giving the number of photoelectrons $N_{pe}(x, y, z)$ produced by 1 MeV energy deposition at point (x, y, z) ("3D light nonuniformity function"). In the following discussion we limit ourselves to the linear one-dimensional variations of the detected light output separable in the axial and transverse directions:

$$N_{pe}(z,x) \propto \begin{cases} N_1 + a_{z1} \cdot z + a_t(z) \cdot x, & z \leq 10 \text{ cm, and } x = \pm 15 \text{ cm} \\ N_2 + a_{z2} \cdot z + a_t(z) \cdot x, & z \geq 10 \text{ cm, and } x = \pm 15 \text{ cm} \end{cases} \quad (14)$$

where a_z (a_t) is the linear optical nonuniformity coefficient in the z (x) coordinate, and the coordinate system origin is at the center of the detector front face.

The simple and straightforward parameterization of the detector light response nonuniformity can be made on the basis of scatter plots showing the light output per unit pathlength as a function of longitudinal or transverse cosmic muon-CsI crystal intersection coordinates. In this analysis we take only cosmic muon events with almost perpendicular trajectories ($\theta_z \geq 85°$), so that the measured two-dimensional light outputs are averaged over the pathlengths and over $\sim$1 cm^2 horizontal cross section areas. The cosmic muons deposit the energy along the well defined ionization track of the length d in the crystal. This description will somewhat underestimate the real light collection probabilities (see Sec. 10) due to the integration of a three-dimensional light nonuniformity function along the charged particle track. The attempt at the full 3D reconstruction of the scintillator light response will be presented in a forthcoming publication [22].

Fig. 13 shows the axial variation of normalized ADC values as a function of distance of energy deposition from the front crystal face for the six representative crystals. The axial positions were calculated by averaging two z values of the cosmic muon track intersection with the crystal surfaces.

Panels on Figs. 14 and 15 show the transverse dependence of measured light output per unit pathlength, where the independent variable is the distance from the crystal axis measured in the horizontal plane. The selected scatter plots show the data points for the axial slices at z_0=6$\pm$1 cm and z_0=18$\pm$1 cm.

We have chosen to parameterize the axial light output nonuniformity with two piecewise linear functions: the light output change $a_{z1}(z \leq 10$ cm) for the front half of the crystal, and the light nonuniformity coefficient for the back half of the crystal $a_{z2}(z \geq 10$ cm), both values expressed in %/cm. The transverse light output variation at a fixed axial distance z_0, $a_t(z_0)$, is described by the average value of a change in luminosity left and right of the crystal axis.

Several general features are readily noticeable: the spread of measured points due to energy deposition straggling, the gradual variation in the collected light along and perpendicular to the detector axis, and the decrease in detected light when the photon generation happens close to lateral detector surfaces and, in particular, near the back corners of the detector volumes.

The calculated ADC/pathlength data points shown on the panels of Figs. 13–15 have been fitted with linear functions imposing the "robust" condition of the minimum absolute deviation between the measured and calculated values, Eqs. 14. The normalized light output scatter plots in the axial and transverse coordinates, as well as two-dimensional ADC/d distributions in the x-z bins and associated linear light output nonuniformity coefficients have been documented for all studied CsI crystals and are available for an inspection at the PIBETA WWW site [23].

In summary, for a set of fifty-nine full hexagonal and pentagonal crystals we find:

- the average axial light nonuniformities are $a_{z1}(z \leq 10$ cm$)=-0.1$%/cm and $a_{z2}(z \geq 10$ cm$)=-1.3$%/cm, respectively (see Fig. 12),
- distribution of nonuniformity coefficients could be described by the $\sigma_{a_{z1}} \approx 1.3$%/cm Gaussian,
- the average transverse light output is flat for $z \leq 10$ cm, but and the typical light variation is -15% at $z=18$ cm,
- the Kharkov crystals on average have twice the axial optical nonuniformity of the Bicron crystals,

For fifteen half-hexagonal and trapezial crystal shapes we find:

- the average axial nonuniformities are $a_{z1}(z \leq 10$ cm$)=-0.3$%/cm and $a_{z2}(z \geq 10$ cm$)=-1.0$%/cm,
- the transverse light output variation is limited in the front crystal half, but increases up to -30% in the back of the crystal.

With the insights gained in the simulation of the light collection probabilities (Sec. 8.2) we conclude that the ± 2%/cm spread of the nonuniformity coefficients corresponds to the equivalent range of 0.8–1.0 crystal surface reflectivities and/or 100–250 cm range of CsI attenuation lengths.

10 Light output uniformity scans of CsI crystals with ^{137}Cs gamma source

A light-tight plywood box was made that fit exactly the size and shape of a single CsI detector. A 0.662 MeV ^{137}Cs gamma source was placed on the top of the box frame and collimated by a $20\times10\times5$ cm^3 lead brick with a 0.6 cm collimator hole. The photomultiplier analog signal from the detector was processed with an ORTEC 454 timing amplifier with a thirty-fold gain and a 50 ns integration time constant. The amplifier output was digitized with a peak sensing ORTEC AD811 ADC unit. The same signal was discriminated and produced the trigger rate of about 5 kHz with a ^{137}Cs source present. The background rate, without the source present, was 50–100 counts/sec.

Pedestal runs were taken with a clock trigger and used to properly correct offsets of the ADC spectra. Temperature variation during one run was less than 0.3°C, typically causing the overall light output variation of less than 0.5% in a ADC spectrum that was gated with 100 ns window. Several runs were taken with the source removed to find the shape of the background spectrum. It was confirmed that the background spectrum does not depend on the position of the lead collimator, so the same background lineshape was used in the analysis for all source positions.

The collimated ^{137}Cs source was placed in turn at five points along the axis of each crystal at 2, 6, 10, 15 and 20 cm from the front face of the crystal.

Following background subtraction, recorded spectra were fitted with a sum of a Gaussian and exponential function, Fig. 16. The peak position and the FWHM for each spectrum were extracted with the statistical uncertainty better than 0.3%.

The dependence of the peak position on the placement of the source is illustrated in Fig. 17 and follows the trend of the tomography results. The `GEANT` simulations revealed that the 662 keV gamma rays could probe all the volume of CsI crystal, but the shower energy deposited at the central axis is only about one-sixth of the energy deposition near the crystal surface. The cosmic muons transfer the energy uniformly along their tracks in CsI material: the scintillation volume over which the measured light output is integrated is therefore larger, and inherent averaging leads to smaller extracted optical nonuniformity coefficients. This feature is borne out in the panels of Fig. 16 where the tomography data for three different crystals yield consistently smaller axial light nonuniformities when compared with the radioactive source measurements.

The simple ^{137}Cs scans with the described apparatus were used to evaluate the light collection nonuniformities for up to six crystals per day.

The radioactive scan measurements similar to ours are described in Refs. [24,33].

11 A GEANT simulation of the PIBETA calorimeter response to 10–120 MeV positrons and photons

We have studied the simulated PIBETA calorimeter response to the 69.8 MeV $\pi^+ \to e^+\nu$ positrons and to the $(69.8+2m_{e^+})$ MeV photons, where m_{e^+} is the positron rest mass. The goal was to find the intrinsic difference between the responses to the monoenergetic positrons and photons with the identical incident total energies, emphasizing the correct modeling of the low-energy tail below the edge of the Michel $\mu \to e^+\nu\nu$ spectrum at 52.8 MeV.

The 0.3% accuracy of the new TRIUMF measurement [4] of the $\pi^+ \to e^+\nu$ branching ratio was limited by the event statistics and systematic uncertainties in evaluating the low-energy tail of the positron peak. The $\pi^+ \to e^+\nu\gamma$ positrons and the forward-peaked bremsstrahlung gammas were detected in a 46-cm-diameter×51-cm-long NaI(Tl) crystal "TINA". The tail correction of (1.44±0.24)% for the energy region from 0 MeV to 52.3 MeV was determined by subtracting the measured Michel positron spectrum from the detector positron response functions measured with the 20–85 MeV e^+ monoenergetic beams. An additional tail component of ∼0.4% due to radiative processes was estimated by Monte Carlo method. The TRIUMF group apparently made no attempt to account for the potential difference in the scintillator light response of positrons and photons and neglected potential nonlinearities of the energy scale. Both effects could arise from the light collection nonuniformities of the NaI(Tl) detector.

In the recent PSI $\pi^+ \to e^+\nu$ experiment [3] the quoted 0.3% systematic uncertainty of the extracted branching ratio was also dominated by the (1.64±0.09)% electromagnetic loss fraction as well as by the (0.95±0.19)% contribution from the photonuclear reactions. The $\sim 4\pi$ calorimeter used in that measurement was made of 132 hexagonally shaped BGO crystals, with the light yield claimed to be homogeneous to within 1.5% over the whole 20 cm length of every crystal.

The lineshapes of positrons and photons in our PIBETA calorimeter and their dependence on the optical properties of 240 constituent CsI crystals were predicted using the GEANT detector description and simulation tools. The code defined the geometry and tracking media for the complete PIBETA detector [63]. The inner detector region was occupied by two cylindrical wire chambers and a segmented plastic veto detector. The incident particles, monoenergetic positrons and photons, were generated in the center of the crystal sphere.

Photonuclear reactions in the active detectors as well as in the surrounding passive material were modeled in a user subroutine [64] that was added to the default `GEANT` version `3.21`. The probabilities of photonuclear reactions were calculated using the published cross sections from the γN reaction thresholds up to the energy of 120 MeV [65–70].

The 240 individual CsI module shapes were specified, taking into account the mechanical tolerances of the physical CsI crystals, with teflon and aluminized Mylar wrappings filling the 200 μm intermodule gaps. The irregular CsI modules had to be constructed from up to six `GEANT` generalized trapezoidal wedges. Every CsI crystal volume was considered a sensitive detector with the associated luminosity $\bar{N}_{pe}$ expressed as a number of photoelectrons per MeV, and two axial and one transverse light collection nonuniformity coefficients, a_{z1}, a_{z2}, and a_t, respectively. A set of seventy-four detector luminosity and nonuniformity values, extracted in the tomography analysis, were initialized in the `GEANT`-accessible database. The optical parameters of the remaining 163 modules were drawn randomly from the distributions in Figs. 9 and 12. The assumption was that the crystals produced in the future will be of the same optical quality as the ones that are already delivered.

We have always simulated at least 10^5 events for every fixed set of the calorimeter parameters ($\bar{N}_{pe}$,a_{z1},a_{z2},a_t). The low-threshold trigger was defined by requiring a sum of the ADC readings exceed 5 MeV of the light-equivalent energy for one calorimeter supercluster containing 32 crystals. The integrated detector acceptances with a low-level trigger were 85.8% for ~70 MeV positrons and 85.5% for ~70 MeV photons, so all extracted quantities had the relative statistical uncertainties of ~0.2%. The response of the calorimeter was parameterized by the FWHM of the simulated ADC spectrum and the tail contribution being between the adjustable low level (default `LT` being 5 MeV) and high level thresholds (two default values $\mathtt{HT}_1$ and $\mathtt{HT}_2$ being 54 MeV and 55 MeV, respectively).

For the comparison and gain normalization purposes we first studied the response of an ideal, homogeneous calorimeter, with the realistic CsI crystal light outputs. The "software" gain factor of every individual CsI detector was determined from the fitted peak positions of the simulated ADC spectrum sum over the crystal with maximum energy deposition and its nearest neighbors. The peak value positions were found after smoothing the histograms with a multiquadric function, to improve on the limited simulation statistics. The ratios of peak positions in the ideal, homogeneous calorimeter and the corresponding values for the physical, nonuniform calorimeter, were, by definition, the individual detector gain corrections. The values of these ratios were refined in three steps of the iterative procedure. The extracted energy resolution of the nonuniform detector in principle depends on the convergence of the gain-matching process and the resulting uncertainties of the individual detector gains. That gain-matching process was equivalent to the PMT high voltage adjustments in the real experiment that are effected to obtain the best energy resolution with the modular detector. We estimate that our simulation procedure fixes the software detector gains with the accuracy of $\sim$1%.

The particular gain constants depended on the optical properties of our CsI crystals as define in our `GEANT` database, but also upon the beam particle chosen in the Monte Carlo calibration runs and its incident energy because of the different shower developments. The calorimeter gain normalizations were calculated using the simulated $\pi^+ \to e^+\nu$ positron peak positions. Due to the gain renormalization, the influence of transverse light nonuniformities smaller than 10% on the ADC spectrum peak positions and the ADC lineshape could be neglected in comparison with the axial light nonuniformity effects. The simulated ADC values were summed over all detectors with the energy deposition above the 1 MeV TDC threshold. We also examined the calculated ADC sums for the clusters which contained the crystal with the maximum energy deposition and its nearest neighbors. The full-widths at half maximum for these spectra are labeled in the following figures and tables as $\mathrm{FWHM}_{(220)}$ and $\mathrm{FWHM}_{(\mathrm{NN})}$, respectively. No event-to-event uncertainties of the ADC pedestal values were assumed in the simulation. Stability of PIBETA electronics tested under real experimental conditions in 1996 calibration runs and the quality of the algorithms used for the first and second pedestal correction reduces the pedestal peak root-mean-square to $\sim$8 channels, equivalent to $\sim$0.3 MeV.

The `GEANT`-calculated resolution of the PIBETA calorimeter consisting of 220 CsI detector crystals and 20 veto crystals was parameterized by the fractional full width at half maximum:

$$\frac{\mathrm{FWHM}_{(220)}}{E_{e^+}}(\%) = \frac{2.36 \cdot \sigma_{E_{e^+}}}{E_{e^+}} = \tag{15}$$

$$= \begin{cases} \frac{54.69+1.197E_{e^+}+0.4656\cdot 10^{-2}E_{e^+}^2}{E_{e^+}^{0.8030}}, & a_{z1,z2}=0 \\ \frac{37.19+0.5983\cdot 10^{-1}E_{e^+}+0.2734\cdot 10^{-2}E_{e^+}^2}{E_{e^+}^{0.5256}}, & a_{z1,z2}=\mathtt{TOMOGRAPHY} \end{cases} \tag{16}$$

for the positrons with the most probable peak energy E_{e^+} MeV and

$$\frac{\mathrm{FWHM}_{(220)}}{E_\gamma}(\%) = \begin{cases} \frac{37.07+0.5507E_\gamma+0.3233\cdot 10^{-2}E_\gamma^2}{E_\gamma^{0.6549}}, & a_{z1,z2}=0 \\ \frac{40.52+0.9437\cdot E_\gamma+0.4931\cdot 10^{-2}E_\gamma^2}{E_\gamma^{0.6942}}, & a_{z1,z2}=\mathtt{TOMOGRAPHY} \end{cases} \tag{17}$$

for the monoenergetic photons with the detected peak energy E_γ MeV (Fig. 18). The a_z=0 lines refer to the cases of an optically uniform detector while the a_z=`TOMO` equations describe the predicted response of the nonuniform calorimeter.

The average fractional energy resolution FWHM$_{(220)}$ of 5.3% (6.0%) was achieved for the $\sim$70 MeV kinetic energy positrons in the optically uniform (nonuniform) calorimeter, as compared to 5.7% (6.8%) resolution for the equivalent energy photons. That was the resolution found with no cuts applied on the light-equivalent energy generated in the calorimeter vetoes. Requiring less than 5 MeV detected in the veto shield decreased the statistics by about 10% and suppressed a low-energy tail, but did not improve the energy resolution at the peak position.

Limiting the ADC sums to the nearest-neighbor crystals (six or seven crystal clusters) the average fractional FHWM$_{(\mathrm{NN})}$ resolution could be parameterized by:

$$\frac{\mathrm{FWHM}_{(\mathrm{NN})}}{E_{e^+}}(\%) = \begin{cases} \frac{69.19+3.057E_{e^+}+0.4198\cdot 10^{-2}E_{e^+}^2}{E_{e^+}^{0.8560}}, & a_{z1,z2}=0 \\ \frac{68.13+2.479E_{e^+}+0.3368\cdot 10^{-2}E_{e^+}^2}{E_{e^+}^{0.8018}}, & a_{z1,z2}=\texttt{TOMOGRAPHY} \end{cases} \quad (18)$$

for the positrons with the detected peak energy E_{e^+} MeV and

$$\frac{\mathrm{FWHM}_{(\mathrm{NN})}}{E_{\gamma}}(\%) = \begin{cases} \frac{43.16+2.318E_{\gamma}+0.4148\cdot 10^{-2}E_{\gamma}^2}{E_{\gamma}^{0.7723}}, & a_{z1,z2}=0 \\ \frac{39.57+2.302E_{\gamma}+0.1329\cdot 10^{-2}E_{\gamma}^2}{E_{\gamma}^{0.7199}}, & a_{z1,z2}=\texttt{TOMOGRAPHY} \end{cases} \quad (19)$$

for the monoenergetic photons with the detected peak energy E_γ MeV (Fig. 19).

The average FWHM$_{(\mathrm{NN})}$ for the 70 MeV positrons and gammas in nearest-neighbor nonuniform crystal clusters was 8.7% (6.1 MeV) and 9.9% (6.8 MeV), respectively. Imposing the 5 MeV cut on the detector veto signals improves these resolutions only marginally. These numbers should be compared with the response width of the ideal uniform nearest-neighbor clusters: 8.2% (5.7 MeV) and 8.7% (6.2 MeV).

The percentage of the events in the tail between the preset low and high energy threshold was tracked in the same `GEANT` simulation.

The listing of the low-energy tail contributions for 69.8 MeV e^+ and 70.8 MeV γ in Table 3 shows that in the optically uniform calorimeter they differ by 1.8%. The optical nonuniformity does not change the positron tail contribution, but increases the photon tail by $\sim$0.2%. The imposition of the 5 MeV veto-shield cut decreases the electromagnetic leakage to 2.4% for positrons and 4.7% for photons, a e^+-γ tail difference of +2.3%.

Table 4 shows the low-energy tail components for the simulated nearest-neighbor cluster ADC sums: with no applied cuts the contributions were 4.7%

and 6.7% for e^+'s and γ's, respectively. The veto shielding cuts decreased both fractions by about 0.3%.

If the positron originates from a radiative $\pi^+ \to e^+ \nu \gamma$ decay, its average Monte Carlo peak position is essentially unchanged. Its tail contribution is unaffected if simulated ADC sums extend over full calorimeter but are increased by $\sim$1.4% if only the nearest-neighbor clusters are summed. The radiative decay matrix elements used in the calculation were taken from Ref. [60]. All quoted numbers have an estimated systematic uncertainty of $\sim$0.2%.

The detector response to positrons and photons in the energy range between 10 MeV and 120 MeV is also nonlinear because the volume distribution of the shower energy deposition depends on the incident particle type and the energy. The `GEANT` studies showed that the magnitude and energy dependence of these nonlinearities does not change significantly because of CsI crystal light collection nonuniformity. Results of the calculations, both for the case of a homogeneous and optically nonhomogeneous calorimeter, are displayed in the Figs. 20 and 21.In covered energy range the detector response nonlinearities for the positrons and photons are very close in the magnitude and shape of energy variation and amounted to $\sim$1.5% for the ADC sums over 220 crystals and up to $\sim$2.8% if the simulated ADC sums were restricted to the over-the-threshold ADCs of nearest neighbors.

12 Conclusion

We measured the optical properties of seventy-four pure cesium iodide crystals that were polished and wrapped in the diffuse Teflon reflector. The results are summarized separately for the full-sized and half-sized crystals in Tables 1 and 2.

The deduced light yields and two axial and one transverse light collection nonuniformity coefficients constitute a minimum set of parameters necessary for a realistic Monte Carlo simulation of the modular calorimeter.

The predicted energy resolutions $\mathrm{FWHM}_{(220)}$ for $\sim$70 MeV positrons and photons in the full PIBETA calorimeter with the ideal, optically uniform CsI modules with specified luminosities were shown to be close, 3.7 MeV and 4.0 MeV, respectively. The upper limit of the low energy tail contributions in the region between 5 and 55 MeV were calculated to be 6.9% and 8.7% for the positrons and gammas in an optically homogeneous detector, respectively. After applying the 5 MeV calorimeter veto cut, these tail corrections decrease to 2.2% and 4.5%.

The average deduced axial light nonuniformities of real CsI crystals wrapped in a Teflon sheet had negative slopes, $-0.18\%/\mathrm{cm}$ and $-1.6\%/\mathrm{cm}$, for the front and back half of the crystal volume, respectively. The corresponding `GEANT` simulation of the nonuniform PIBETA apparatus for 68.9 MeV e^+ and 70.8 MeV γ's shows that both energy responses will be broadened to the average $\mathrm{FWHM}_{(220)}$ of 5.9% and 6.9% while the associated tail contributions will change only for photon spectra, increasing a low-energy tail by $\sim$0.3%.

The nonlinearity of the measured energy scale caused by the optical nonuniformity is $\leq$2.8% throughout the relevant e^+/γ energy range. This spread is consistent with the precision of energy calibration required to extract the tail corrections with the systematic uncertainty of $\sim$0.2%.

The predicted ADC spectra of the monoenergetic positrons, electrons and tagged photons in the energy range 10–70 MeV will be compared with the measured responses of the partial CsI calorimeter arrays in the forthcoming publication [71].

References

[1] D. Počanić, D. Day, E. Frlež, R. M. Marshall, J. S. McCarthy, R. C. Minehart, K. O. H. Ziock, M. Daum, R. Frosch and D. Renker, PSI R-89.01 Experiment Proposal (Paul Scherrer Institute, Villigen, 1988).

[2] W. K. McFarlane, L. B. Auerbach, F. C. Gaille, V. L. Highland, E. Jastrzembski, R. J. Macek, F. H. Cverna, C. M. Hoffman, G. E. Hogan, R. E. Morgado and R. D. Werbeck, Phys. Rev. D32 (1985) 547.

[3] G. Czapek, A. Federspiel, A. Fluckiger, D. Frei, B. Hahn, C. Hug, E. Hugentobler, W. Krebs, U. Moser, D. Muster, E. Ramseyer, H. Scheidiger, P. Schlatter, G. Stucki, R. Abela, D. Renker and E. Steiner, Phys. Rev. Lett. 70 (1993) 17.

[4] D. I. Britton, S. Ahmad, D. A. Bryman, R. A. Burnham, E. T. H. Clifford, P. Kitching, Y. Kuno, J. A. Macdonald, T. Numao, A. Olin, J. M. Poutissou and M. S. Dixit, Phys. Rev. D49 (1994) 28.

[5] A. Sirlin, Rev. Mod. Phys. **50** (1978) 573.

[6] A. Sirlin, private communication (1989).

[7] I. S. Towner and J. C. Hardy, Currents and Their Couplings in the Weak Sector of the Standard Model, NUCL-TH/9504015 Preprint (1995).

[8] W. J. Marciano and A. Sirlin, Phys. Rev. D35 (1987) 1672.

[9] R. B. Murray and F. J. Keller, Phys. Rev. 137A (1965) A942.

[10] C. W. Bates, A. Salau, and D. Leniart, Phys. Rev. B15 (1977) 5963.

[11] H. Kobayashi, A. Konaka, K. Miyake, T. T. Nakamura, T. Nomura, N. Sasao, T. Yamashita, S. Sakuragi, and S. Hashimoto, Kyoto University Preprint KUNS-900 (1987).

[12] S. Kubota, H. Murakami, J. Z. Ruan, N. Iwasa, S. Sakuragi, and S. Hashimoto, Nucl. Inst. and. Meth. A273 (1988) 645.

[13] S. Kubota, S. Sakuragi, S. Hashimoto and J. Z. Ruan, Nucl. Inst. and Meth. A268 (1988) 275.

[14] S. Keszthelyi-Lándori, I. Földvári, R. Voszka, Z. Fodor, and Z. Seres, Nucl. Inst. and Meth. A303 (1991) 374.

[15] C. L. Woody, P. W. Levy, J. A. Kierstead, T. Skwarnicki, Z. Sobolewski, M. Goldberg, N. Horwitz, P. Souder and D. F. Anderson, IEEE Trans. Nucl. Sci. 37 (1990) 492.

[16] P. Schotanus, R. Kamermans and P. Dorenbos, IEEE Trans. Nucl. Sci. 37 (1990) 177.

[17] B. K. Utts and S. E. Spagno, IEEE Trans. Nucl. Sci. 37 (1990) 134.

[18] A. V. Gektin, A. I. Gorelov, V. I. Rykalin, V. I. Selivanov, N. V. Shiran, and V. G. Vasilchenko, Nucl. Inst. and Meth. A294 (1990) 591.

[19] M. M. Hamada, Y. Nunoya, S. Kubota, and S. Sakuragi, Nucl. Inst. and. Meth. A365 (1995) 98.

[20] C. Woody, BNL-47776-MC (1992).

[21] Z. Y. Wei and R. Y. Zhu, Nucl. Inst. and Meth. A326 (1993) 326.

[22] E. Frlež, S. Ritt, K. A. Assamagan, Ch. Brönnimann, T. Flügel, B. Krause, D. Počanić, D. Renker, P. L. Slocum, N. Soić, I. Supek, *Three-Dimensional Reconstruction of Light Collection Probability Function for Pure CsI Scintillators*, to be submitted to Nucl. Phys. and Meth.

[23] The PIBETA Decay Experiment Home Page, accessible at URL `http://helena.phys.virginia.edu/~pibeta/` or `http://psw340.psi.ch/~pibeta/`, (1997).

[24] J. Brose, G. Dahlinger, P. Eckstein, K. R. Schubert and R. Seitz, SLAC BaBar Note #175, Stanford (1995).

[25] G. Dahlinger, SLAC BaBar Note #241, Stanford (1996).

[26] C. Morris and R. L. Boudrie, A Proposal for a High Resolution Spectrometer for Neutral Mesons (LAMPF, Los Alamos, 1989).

[27] R. E. Ray, FERMILAB-CONF-94-418 (1994).

[28] R. S. Kessler, A. Roodman, P. Shawhan, N. Solomey, B. Winstein, S. Hansen, H. Nguyen, R. Ray, R. Tschirhart, J. Whitmore, T. Nakaya, and M. Lindgren, Nucl. Inst. and Meth. A368 (1996) 653.

[29] G. David, A. Hershcovitch, S. Stoll, C. Woody, P. B. Munzinger, R. Hutter, J. Stachel, C. M. Zou, N. Horwitz, and Z. Sobolewski, Nucl Inst. and Meth. A348 (1994) 87.

[30] H. Kenner, Geodesic Math and How to Use It (University of California Press, Berkeley, 1976).

[31] Review of Particle Physics, Particle Data Group, Phys. Rev. D54 (1996) 72.

[32] K. A. Assamagan, Ph. D. Thesis (University of Virginia, Charlottesville, 1995) unpublished.

[33] D. H. Dowell, A. M. Sandorfi, A. Q. R. Baron, B. J. Fineman, O. C. Kistner, G. Matone, C. E. Thorn, and R. M. Sealock, Nucl. Instr. and Meth. A286 (1990) 183.

[34] H. Grassman and H. G. Moser, Nucl. Instr. and Meth. A237 (1985) 486.

[35] THORN-EMI Electron Tubes Catalog: Photomultipliers and Accessories, Rockaway, NJ (1993).

[36] C. L. Smith, PMT Evaluation PIBETA Note, accessible at URL `http://helena.phys.virginia.edu/~pibeta/` or `http://psw340.psi.ch/~pibeta/`, (1995).

[37] E. Frlež, Ch. Brönnimann, T. Flügel, J. E. Koglin, B. Krause, D. Počanić, D. Renker, S. Ritt, P. L. Slocum, *"The Light Response of Pure CsI Calorimeter Crystals Painted with Waveshift Lacquer"*, to be submitted to Nucl. Phys. and Meth.

[38] L. G. Atencio, J. F. Amann, R. L. Boudrie and C. L. Morris, Nucl. Inst. and Meth. 187 (1981) 381.

[39] C. L. Morris, Nucl. Inst. and Meth. 196 (1982) 263.

[40] R. D. Ransome, Ph. D. Thesis, LA-8919-T (LAMPF, Los Alamos, 1981).

[41] R. D. Ransome, S. J. Greene, C. L. Hollas, B. E. Bonner, M. W. McNaughton, C. L. Morris and H. A. Thiessen, Nucl. Inst. and Meth. 201 (1982) 309.

[42] A. H. Walenta, Nucl. Inst. and Meth. 151 (1978) 461.

[43] G. A. Erskine, Nucl. Inst. and Meth. 198 (1982) 325.

[44] D. Brown and E. Sandler, Drift Chamber Electronics, LAMPF E-Division Semiannual Report LA-8069-PR (1979) 63.

[45] S. Ritt, Data Acquisition PIBETA Note, accessible at URL `http://helena.phys.virginia.edu/~pibeta/` or `http://psw340.psi.ch/~pibeta/`, (1995).

[46] F. James and M. Roos, MINUIT—Function Minimization and Error Analysis, CERNLIB D506 (CERN, Geneva, 1989).

[47] M. W. McNaughton, Introduction to the LAMPF Recoil Polarimeter (Janus) MP-13/MWM/X87-01 (LAMPF, Los Alamos, 1987).

[48] I. Supek, Ph. D. Thesis, (LAMPF, Los Alamos, 1989) unpublished.

[49] R. Brun, F. Bruyant, M. Maire, A. C. McPherson and P. Zanarini, `GEANT` 3.21 DD/EE/94-1 (CERN, Geneva, 1994).

[50] R. Brun, O. Couet, C. Vandoni, P. Zanarini and M. Goossens, PAW 2.03—Physics Analysis Workstation CN/Q121 (CERN, Geneva, 1993).

[51] W. R. Leo, Techniques for Nuclear and Particle Physics Experiments, (Springer-Verlag, New York, 1987).

[52] P. J. Huber, Robust Statistics (Wiley, New York, 1981).

[53] W. H. Press, B. P. Fannery, S. A. Teukolsky and W. T. Vetterling, Numerical Recipes—Art of Scientific Computing (Cambridge University Press, Cambridge, 1986).

[54] LeCroy 1995 Research Instrumentation Catalogue (Chestnut Ridge, NY, 1995).

[55] B. Rossi, Rev. Mod. Phys. 20 (1948) 537.

[56] B. K. Wright, Program OPTICS (University of Virginia, Charlottesville, 1992), unpublished.

[57] B. K. Wright, Program TkOptics (University of Virginia, Charlottesville, 1994), unpublished.

[58] J. K. Ousterhout, Tck and Tk Toolkit (Addison-Wesley, Melno Park, 1994).

[59] E. Frlež, Measurement of Bulk CsI Index of Refraction and Attenuation Length (University of Virginia, Charlottesville, 1989), unpublished.

[60] S. G. Brown and S. A. Bludman, Phys. Rev. 136 (1964) 1160.

[61] G. Källén, Elementary Particle Physics (Addison-Wesley, Palo Alto, 1964).

[62] E. S. Ginsberg, Phys. Rev. 142 (1966) 1035.

[63] The PIBETA Collaboration, Status Update of PSI Experiment R-89.01.1 (Paul Scherrer Institute, Villigen, 1995) unpublished.

[64] E. Frlež, Photonuclear Reactions in GEANT Code, accessible at URL http://helena.phys.virginia.edu/~pibeta/ or http://psw340.psi.ch/~pibeta/, (1995).

[65] J. Ahrens, H. Borchert, K. H. Czock, H. B. Eppler, H. Gimm, H. Gundrun, M. Kröning, P. Riehn, G. Sita Ram, A. Zieger and B. Ziegler, Nucl. Phys. A251 (1975) 478.

[66] A. Lepretre, H. Beil, R. Bergère, P. Carlos, J. Fagot, A De Miniac and A. Veyssière, Nucl. Phys. A367 (1981) 237.

[67] H. Hebach, A. Wortberg, and M. Gari, Nucl. Phys. A267 (1976) 425.

[68] B. L. Berman, R. L. Bramblett, J. T. Caldwell, H. S. Davis, M. A. Kelly and S. C. Fultz, Phys. Rev. 177 (1969) 1745.

[69] R. L. Bramblett, J. T. Caldwell, B. L. Berman, R. R. Harvet and S. C. Fultz, Phys. Rev. 148 (1966) 1198.

[70] G. G. Jonsson and B. Forkman, Nucl. Phys. A107 (1968) 52.

[71] E. Frlež, K. A. Assamagan, Ch. Brönnimann, T. Flügel, J. E. Koglin, B. Krause, D. W. Lawrence, R. C. Minehart, D. Počanić, D. Renker, B. G. Ritchie, S. Ritt, P. L. Slocum, and I. Supek, *"The Response of the PIBETA CsI Calorimeter Array to 10–70 MeV Positrons, Electrons and Tagged Photons"*, to be submitted to Nucl. Phys. and Meth.

Fig. 1. The PIBETA CsI shower calorimeter consists of 240 tapered hexagonal, pentagonal and trapezial pyramids. The crystal ball has an opening for beam entry and a symmetric one for light readout from inner detectors (not shown).

Fig. 2. The fast-to-total light component ratio for the all studied CsI crystals. The light outputs from optically polished and unwrapped crystals were measured immediately after the crystals were received from manufacturer with a digital oscilloscope at the average ambient temperature of 22°C.

Fig. 3. Monte Carlo simulation of penetrating cosmic muons interacting with the experimental apparatus. Six CsI crystals were defined inside the dark box and deposited energies and track lengths of cosmic muons and generated secondary particles in detectors were digitized.

Fig. 4. The schematic diagram of the electronics logic for the tomography apparatus. The calibration event was triggered by two-fold scintillator coincidence S1×S2. The trigger used during cosmic muon data acquisition required three-fold coincidence between two scintillators and at least one CsI detector, $(\mathrm{S1}\times\mathrm{S2})\times\sum \mathrm{CsI}_i$.

Fig. 5. One-dimensional residuals defined as differences between the best straight line fits from the reconstructed coordinates in the hit chambers 1 and 2 and the measured positions in the top chamber 3. The FWHM of the peak is 0.9 mm for x coordinate and 1.5 mm for y coordinate, respectively. The 1.2 cm wide plateaus contains ∼5% events with incorrect left-right identification and/or the events undergoing the large angle scattering in the apparatus.

Fig. 6. The average measured cosmic muon pathlength in the CsI crystals was ∼6 cm. In order to accurately determine the track length, the precise knowledge of the absolute crystal position with respect to drift chambers was required. Number of muon tracks intersecting a CsI crystal volume is shown as a function of horizontal crystal offsets. Contours of the 25-level plot reveal a crystal position with an uncertainty of ±0.05 cm (left panel, pentagonal CsI crystal: $x_{\mathrm{off}} = 12.32\pm0.05$ cm, $z_{\mathrm{off}} = 30.50\pm0.05$ cm). The same type of plot is shown for one hexagonal CsI crystal on the right panel.

Fig. 7. Fast light output temperature coefficients for all analyzed CsI calorimeter detectors. The mean value is $-1.4\%/^\circ$C, with the temperature coefficients ranging from $-4\%/^\circ$C to $+4\%/^\circ$C. Temperature changes inside the light-tight box (filled markers) and average ADC values (open circles) for one detector with the negative temperature coefficient of $-1.9/^\circ$C are shown in the inset. Data points shown in the inset span one week of data acquisition.

Fig. 8. Photodiode spectra in one CsI detector recorded for five different values of the LED driving voltage. The horizontal scale is a raw ADC count of the fast CsI scintillation component (a 100 ns gate) corrected for the pedestal offset. The equivalent energy range covered is 10–100 MeV. The photoelectron statistics can be determined by measuring the width of the photodiode peak σ_E^2 as a function of a spectrum mean value $\bar{E}$. The linear dependence described by Eq. (6) is demonstrated in the inset. The inverse slope of the straight line equals the number of photoelectrons created per unit energy deposition.

Fig. 9. The number of photoelectrons per MeV of deposited energy for all studied CsI calorimeter modules. The left panel shows the distribution for the full-sized hexagonal and pentagonal CsI detectors viewed with three inch phototubes. The right panel is the equivalent histogram for the smaller half-hexagonal and trapezial detectors equipped with two inch phototubes.

Fig. 10. The simulated light collection probability as a function of axial (z) and transverse (x) coordinates for an optically ideal hexagonal detector (HEX–A) with a two-layer Teflon wrapping. The size of the histogrammed 2D bin is 1×1 cm^2. The average light collection probability with a three inch phototube is 23%.

Fig. 11. The Monte Carlo light collection probability as a two dimensional function of axial and transverse coordinates for an ideal half-hexagonal detector (HEX–D1) with a Teflon wrapping. The average light collection probability with a two inch photocathode is 12%.

Fig. 12. The light nonuniformity coefficients a_{z1} and a_{z2} (%/cm), determined separately for front ($z\leq10$ cm) and back ($z\geq10$ cm) crystal sections, are shown here in a scatter-plot for 74 CsI detectors. The full-sized hexagonal and pentagonal detectors are represented with the full marker points, while the open circles indicate the half-hexagonal and trapezial detector shapes. The dotted line is the result of a "robust" straight-line fit: a_{z1}(%/cm, $z\leq10$ cm)$=-1.44+1.19\cdot a_{z2}$(%/cm, $z\geq10$ cm).

Fig. 13. Relative light per unit pathlength ADC/d as a function of axial position of energy deposition for six CsI crystals. The phototubes were always positioned on the surface with the larger values of the z coordinate. Plotted values were corrected for temperature variation effects and the PMT gain drifts.

Fig. 14. Detected light per unit pathlength as a function of transverse coordinates of energy deposition shown at the fixed distance along the crystal axis (z_0=6±1 cm) for six CsI detectors.

Fig. 15. Detected light per unit pathlength as a function of transverse position of energy deposition shown at the fixed axial distance (z_0=18±1 cm) for six CsI crystals.

Fig. 16. The 662 keV ^{137}Cs gamma source and the background spectrum measured at the source axial position z=10 cm from the front face of the pentagonal S003 crystal.

Fig. 17. The comparison of normalized light output (ADC reading/pathlength) along the axis of three different CsI crystals deduced from the cosmic muon tomography data (full line), and as measured with the ^{137}Cs gamma source scan (dotted line).

Fig. 18. The predicted fractional energy resolution FWHM$_{(220)}/E_{(220)}$ of the PIBETA calorimeter for positrons and photons in the energy range 10–120 MeV. The `GEANT`-deduced relative FWHM$_{(220)}$ for the sum over 220 CsI ADCs is shown both for an ideal homogeneous detector (full lines) as well as for a nonuniform calorimeter (dotted lines). Notice that the zero value on the vertical scale is suppressed. The curves represent the parameterizations quoted in the text.

Fig. 19. The `GEANT`-deduced FWHM$_{(\mathrm{NN})}/E_{(\mathrm{NN})}$ for the sum over nearest-neighbor CsI ADCs is shown both for an ideal homogeneous detector as well as for a nonuniform calorimeter.

Fig. 20. Nonlinearity of the PIBETA calorimeter energy response for positrons and photons in the energy range 10–120 MeV. The ratio of the detected ADC peak position to the incident particle energy is calculated in a `GEANT` simulation. Results for an ideal homogeneous detector and a nonuniform calorimeter are shown separately. The normalization is given by ADC/E(70 MeV e^+, γ)=1.

Fig. 21. Nonlinearity of the PIBETA calorimeter energy response for positrons and photons in the energy range 10–120 MeV. Ratio of the detected peak position of summed nearest-neighbor ADC spectra to the incident particle energy is calculated in a `GEANT` simulation.

Fig. 22. The predicted PIBETA calorimeter spectra of the monoenergetic 69.8 MeV positrons and 70.8 MeV photons. The 220 ADC values above the 1.0 MeV TDC threshold were summed. A `GEANT` simulation assumed different numbers of photoelectrons/MeV and linear axial light collection nonuniformities as extracted in the tomography analysis. The results for the "realistic" detector depend on the treatment of the CsI crystal surfaces and the details of the gain matching algorithm.

Fig. 23. The predicted PIBETA calorimeter spectra of the monoenergetic 69.8 MeV positrons and 70.8 MeV photons. The ADC value for the CsI crystal with the maximum ADC value and the ADC readings of its nearest neighbors were summed. A `GEANT` simulation assumed different numbers of photoelectrons/MeV and linear axial light collection nonuniformities for each detector, as measured in the tomography apparatus.

Table 1
Average scintillation properties of hexagonal and pentagonal PIBETA CsI calorimeter shapes PENTAs, HEX–As, HEX–Bs, HEX–Cs and HEX–Ds (59 crystals). All crystals were polished and wrapped in two layers of a Teflon membrane and one layer of aluminized Mylar film. The light yields are normalized to the temperature of 18°C. All other parameters were measured at the average laboratory room temperature of 22°C.

	BICRON CsI Crystals (22)	Kharkov CsI Crystals (37)
Fast-to-Total Ratio (100 ns/1 μs gate)	0.835	0.739
# Photoelectrons/MeV (100 ns ADC gate)	83.4	65.1
# Photoelectrons/MeV (1 μs ADC gate)	99.9	88.0
Fast Light Temp. Coefficient (%/°C)	−1.20	−1.61
Total Light Temp. Coefficient (%/°C)	−1.25	−1.40
Axial Nonuniformity Coefficient (%/cm), $z \leq 10$ cm, 100 ns ADC gate	−0.200	−0.124
Axial Nonuniformity Coefficient(%/cm), $z \geq 10$ cm, 100 ns ADC gate	−1.62	−1.61
Transverse Nonuniformity Coefficient(%/cm), $z_0=6$ cm, 100 ns ADC gate	−0.400	−0.500
Transverse Nonuniformity Coefficient(%/cm), $z_0=18$ cm, 100 ns ADC gate	−1.10	−1.20

Table 2
Average scintillation properties of half-hexagonal and trapezial PIBETA CsI calorimeter shapes HEX–D1/2s and VETO–1/2s (15 crystals). All crystals were polished and wrapped in two layers of Teflon foil and one layer of aluminized Mylar.

	BICRON CsI Crystals (3)	Kharkov CsI Crystals (12)
Fast-to-Total Ratio (100 ns/1 μs gate)	0.806	0.728
# Photoelectrons/MeV (100 ns ADC gate)	34.5	31.5
# Photoelectrons/MeV (1 μs ADC gate)	42.8	43.3
Fast Light Temp. Coefficient (%/°C)	−2.08	−0.63
Total Light Temp. Coefficient (%/°C)	−1.78	−0.69
Axial Nonuniformity Coefficient (%/cm), $z\leq 10$ cm, 100 ns ADC gate	−0.326	−0.500
Axial Nonuniformity Coefficient(%/cm), $z\geq 10$ cm, 100 ns ADC gate	−1.00	−1.83
Transverse Nonuniformity Coefficient(%/cm), z_0=6 cm, 100 ns ADC gate	−0.755	−0.827
Transverse Nonuniformity Coefficient(%/cm), z_0=18 cm, 100 ns ADC gate	−4.10	−5.14

Table 3
The predicted energy resolutions and tail contributions for 69.8 MeV e^+ and 70.8 MeV γ's events in the full PIBETA calorimeter. The light output in photoelectrons/MeV and the linear axial light collection nonuniformities measured for individual CsI crystals ($a_{z1,z2}$=`TOMOGRAPHY`) were used in a `GEANT` simulation. The values for the perfect optically homogeneous crystals ($a_{z1,z2}$=0) were shown for comparison.

Parameter	69.8 MeV e^+		70.8 MeV γ	
No E_V cut	$a_{z1,z2}$=0	`TOMOGRAPHY` $a_{z1,z2}$	$a_{z1,z2}$=0	`TOMOGRAPHY` $a_{z1,z2}$
Peak Position (MeV)	68.87±0.03	68.90±0.03	70.10±0.03	69.97±0.03
$\mathrm{FWHM}_{(220)}$ (MeV)	3.66±0.03	4.10±0.03	3.98±0.03	4.76±0.03
5≤Events≤54 MeV (%)	6.44±0.09	6.46±0.09	8.20±0.10	8.47±0.10
5≤Events≤55 MeV (%)	6.89±0.09	6.98±0.09	8.86±0.10	9.11±0.11
$E_V \leq 5$ MeV	$a_{z1,z2}$=0	`TOMOGRAPHY` $a_{z1,z2}$	$a_{z1,z2}$=0	`TOMOGRAPHY` $a_{z1,z2}$
Peak Position (MeV)	68.88±0.03	68.92±0.03	70.07±0.03	69.99±0.03
$\mathrm{FWHM}_{(220)}$ (MeV)	3.67±0.03	4.09±0.03	3.99±0.03	4.76±0.03
5≤Events≤54 MeV (%)	1.91±0.05	2.02±0.05	3.92±0.07	4.15±0.07
5≤Events≤55 MeV (%)	2.24±0.05	2.36±0.05	4.46±0.07	4.68±0.07

Table 4
The predicted energy resolutions and tail contributions for 69.8 MeV e^+ and 70.8 MeV γ's events in the PIBETA clusters containing the crystal with maximum energy deposition and its nearest neighbors.

Parameter	69.8 MeV e^+		70.8 MeV γ	
No E_V cut	$a_{z1,z2}$=0	`TOMOGRAPHY` $a_{z1,z2}$	$a_{z1,z2}$=0	`TOMOGRAPHY` $a_{z1,z2}$
Peak Position (MeV)	67.74±0.03	67.85±0.03	68.80±0.03	68.65±0.03
$\mathrm{FWHM}_{(\mathrm{NN})}$ (MeV)	5.22±0.03	5.90±0.03	6.01±0.03	6.80±0.03
5≤Events≤54 MeV (%)	3.83±0.07	4.01±0.07	5.47±0.08	5.78±0.08
5≤Events≤55 MeV (%)	4.54±0.07	4.73±0.08	6.33±0.09	6.67±0.09
E_V≤5 MeV	$a_{z1,z2}$=0	`TOMOGRAPHY` $a_{z1,z2}$	$a_{z1,z2}$=0	`TOMOGRAPHY` $a_{z1,z2}$
Peak Position (MeV)	67.75±0.03	67.83±0.03	68.80±0.04	68.64±0.03
$\mathrm{FWHM}_{(\mathrm{NN})}$ (MeV)	5.52±0.03	5.83±0.03	5.92±0.03	6.76±0.03
5≤Events≤54 MeV (%)	3.53±0.07	3.73±0.07	5.28±0.08	5.59±0.08
5≤Events≤55 MeV (%)	4.19±0.07	4.39±0.07	6.10±0.09	6.42±0.09

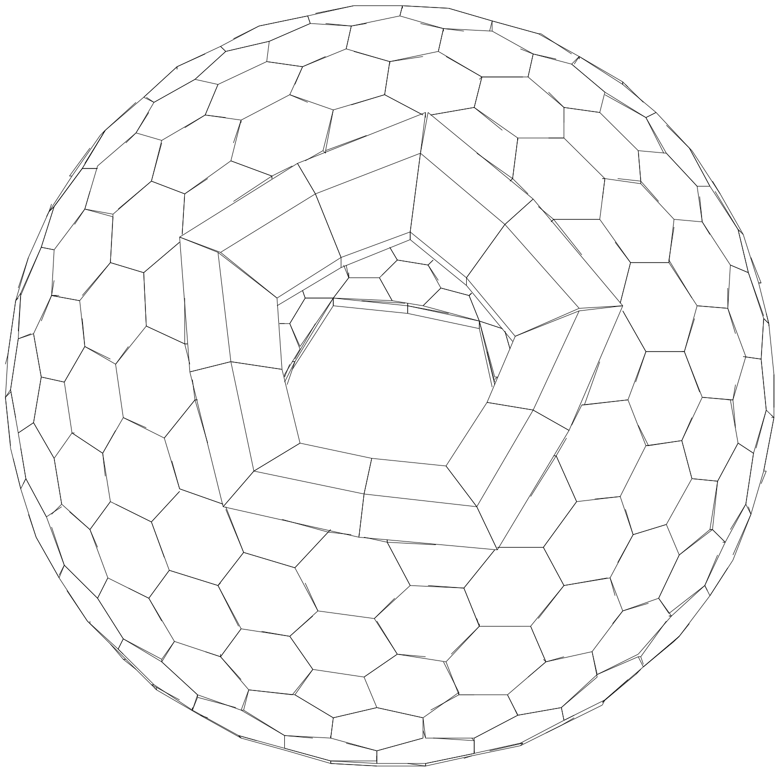

FIGURE 1

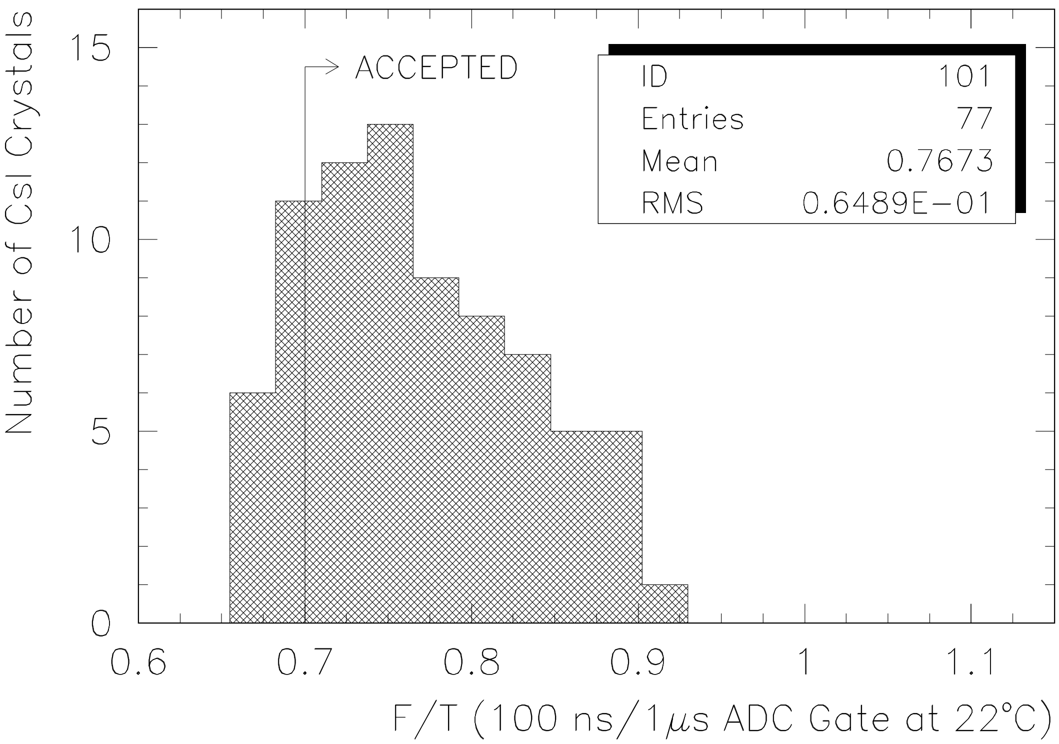
ACCEPTED
ID 101
Entries 77
Mean 0.7673
RMS 0.6489E-01
Number of CsI Crystals
0
5
10
15
0.6
0.7
0.8
0.9
1
1.1
F/T (100 ns/1μs ADC Gate at 22°C)

FIGURE 2

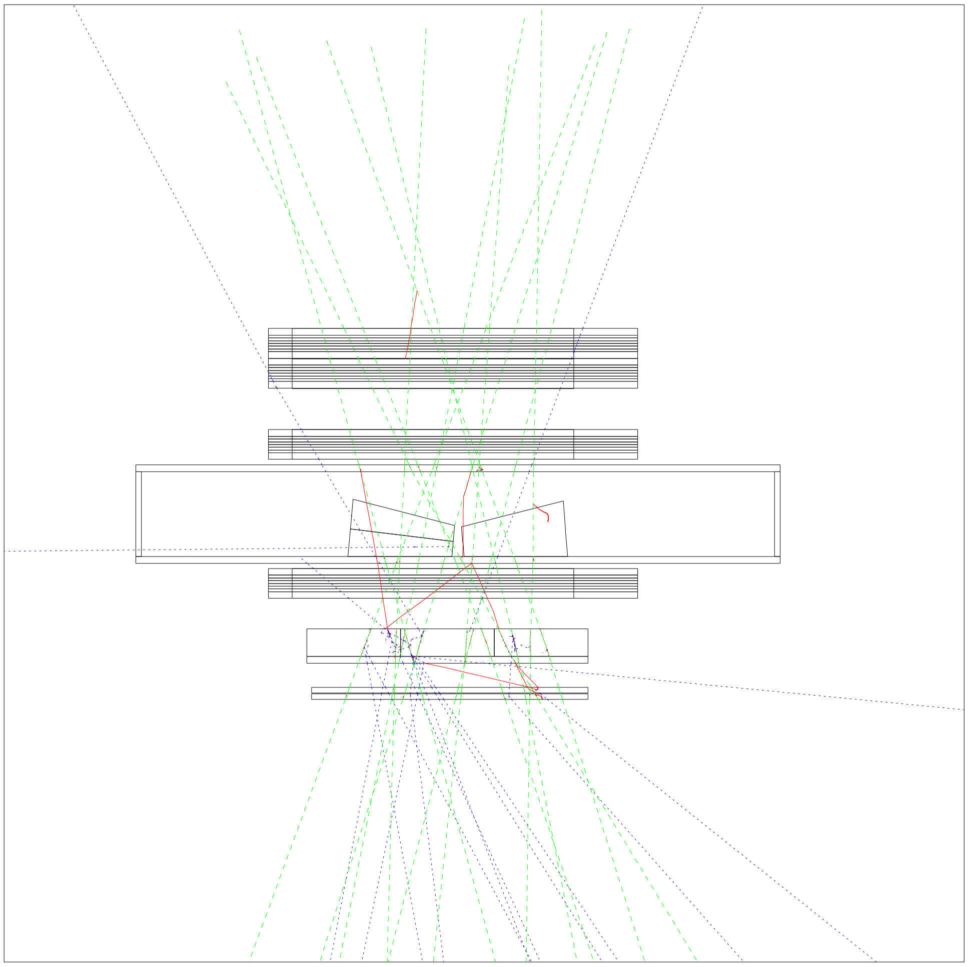

FIGURE 3

FIGURE 4

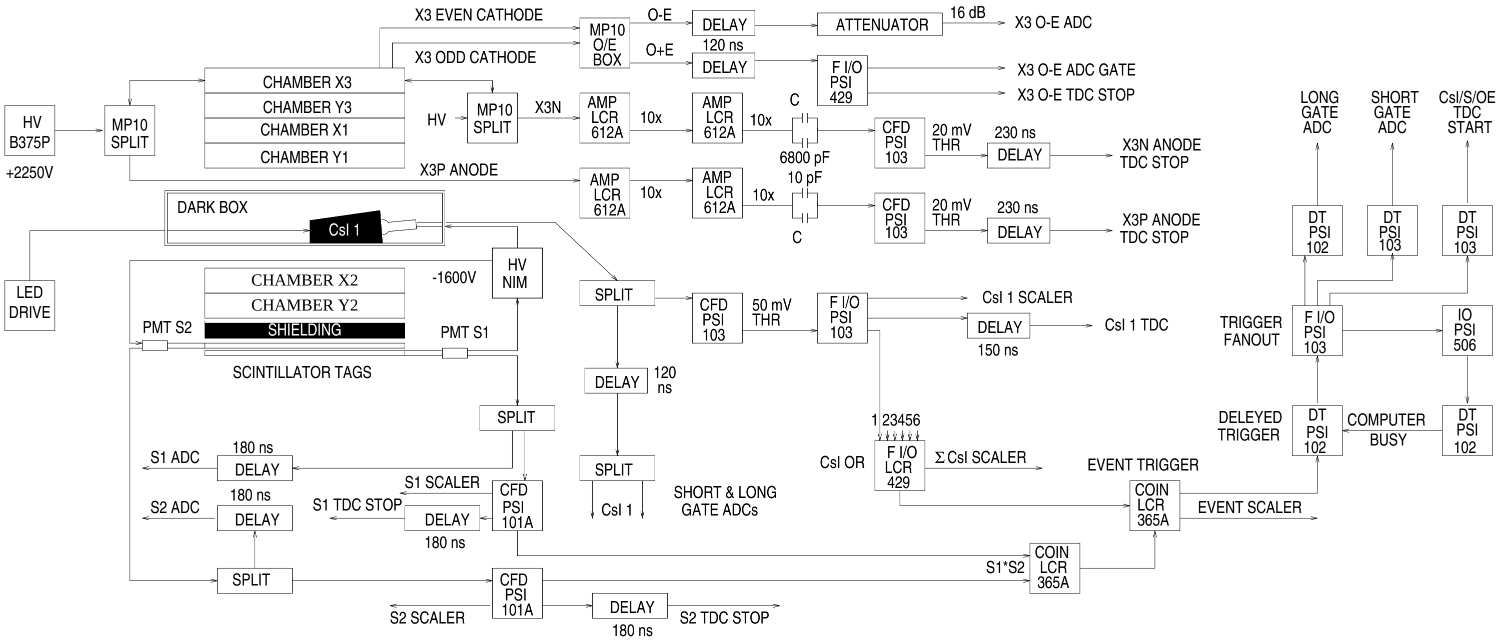

HV = HIGH VOLTAGE
CFD = CONSTANT FRACTION DISCRIMINATOR
AMP = PMT AMPLIFIER
F I/O = FAN IN/OUT UNIT
IO = INPUT/OUTPUT UNIT
COINC = COINCIDENCE UNIT
PMT = PHOTOMULTIPLIER
DT = DELAYED TRIGGER
C = CAPACITOR BOX

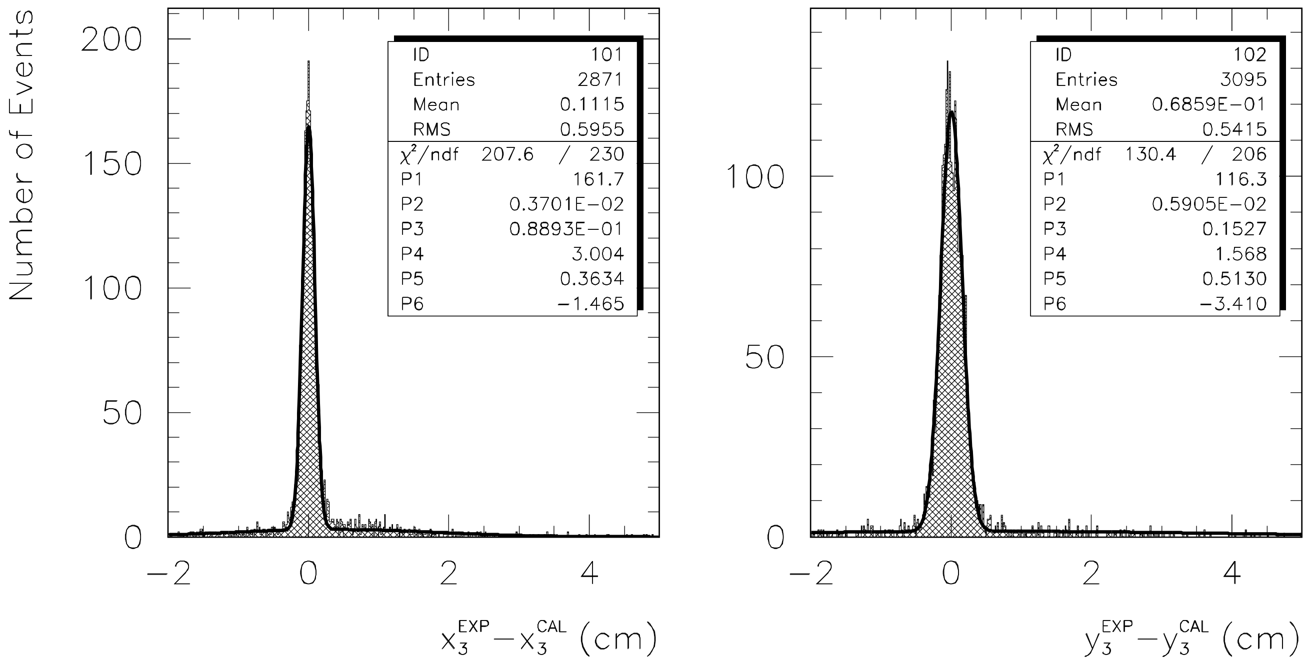

Number of Events
200
150
100
50
0
−2
0
2
4
ID 101
Entries 2871
Mean 0.1115
RMS 0.5955
χ²/ndf 207.6 / 230
P1 161.7
P2 0.3701E−02
P3 0.8893E−01
P4 3.004
P5 0.3634
P6 −1.465
x₃^EXP−x₃^CAL (cm)
100
50
0
−2
0
2
4
ID 102
Entries 3095
Mean 0.6859E−01
RMS 0.5415
χ²/ndf 130.4 / 206
P1 116.3
P2 0.5905E−02
P3 0.1527
P4 1.568
P5 0.5130
P6 −3.410
y₃^EXP−y₃^CAL (cm)

FIGURE 5

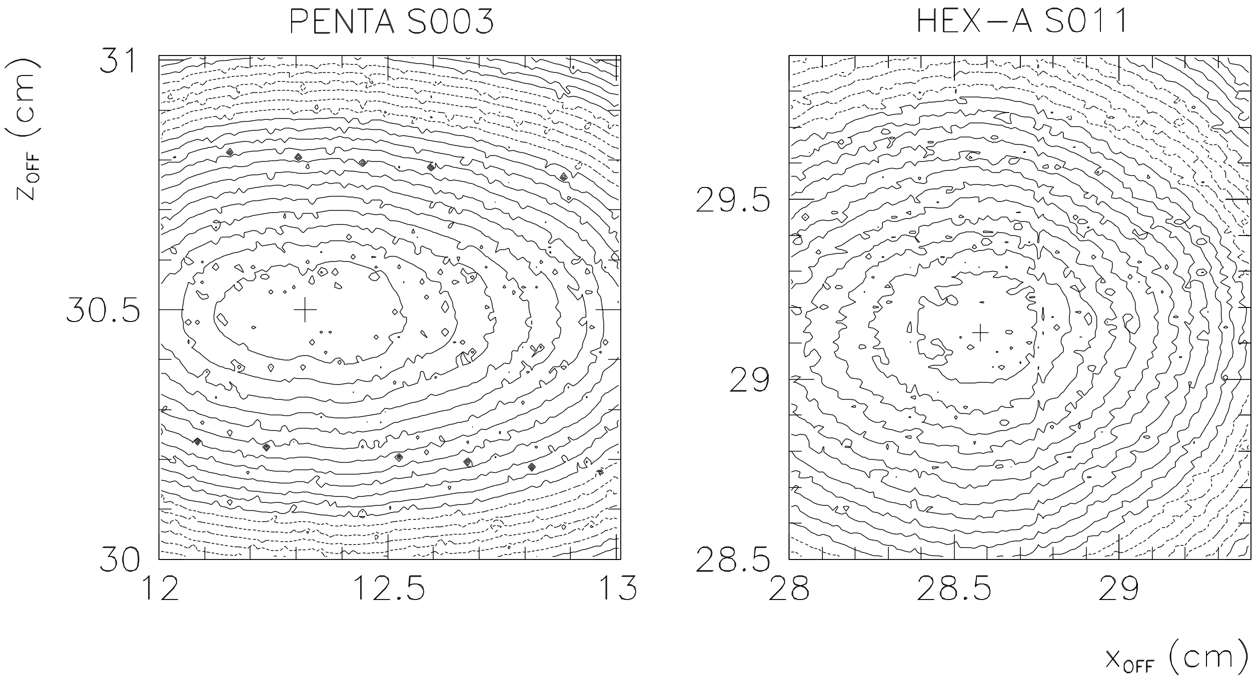
PENTA S003
HEX−A S011
z_{OFF} (cm)
31
30.5
30
12
12.5
13
29.5
29
28.5
28
28.5
29
x_{OFF} (cm)

FIGURE 6

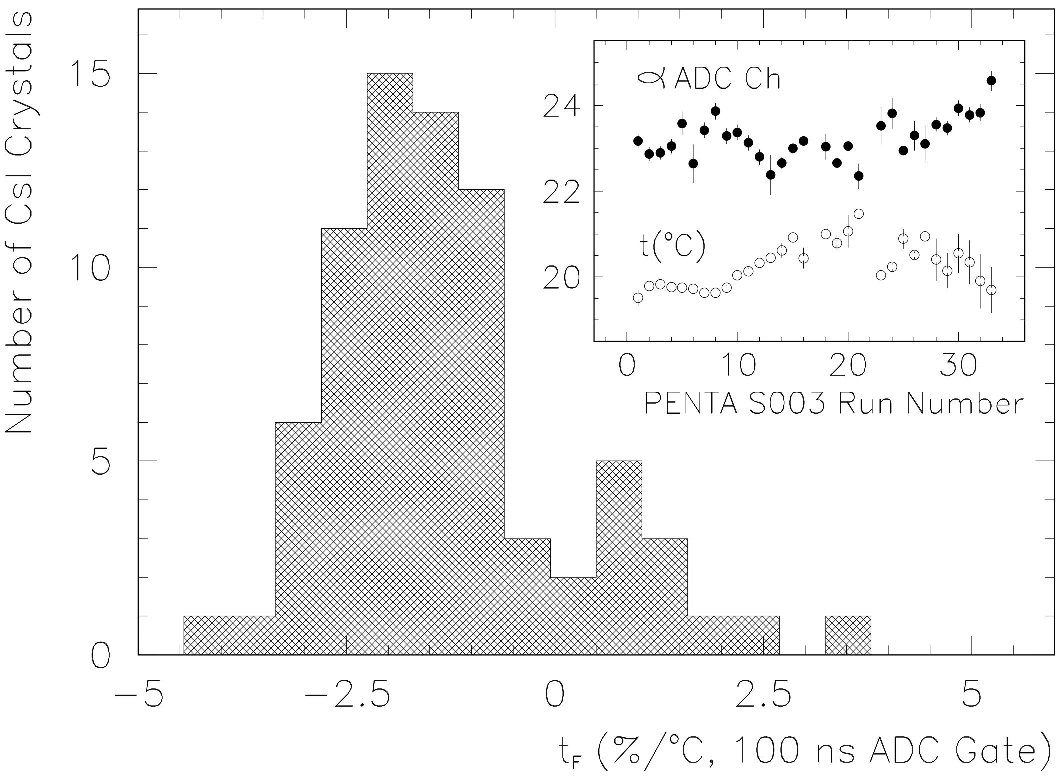
Number of CsI Crystals
15
10
5
0
−5
−2.5
0
2.5
5
t_F (%/°C, 100 ns ADC Gate)
α ADC Ch
24
22
20
t(°C)
0
10
20
30
PENTA S003 Run Number

FIGURE 7

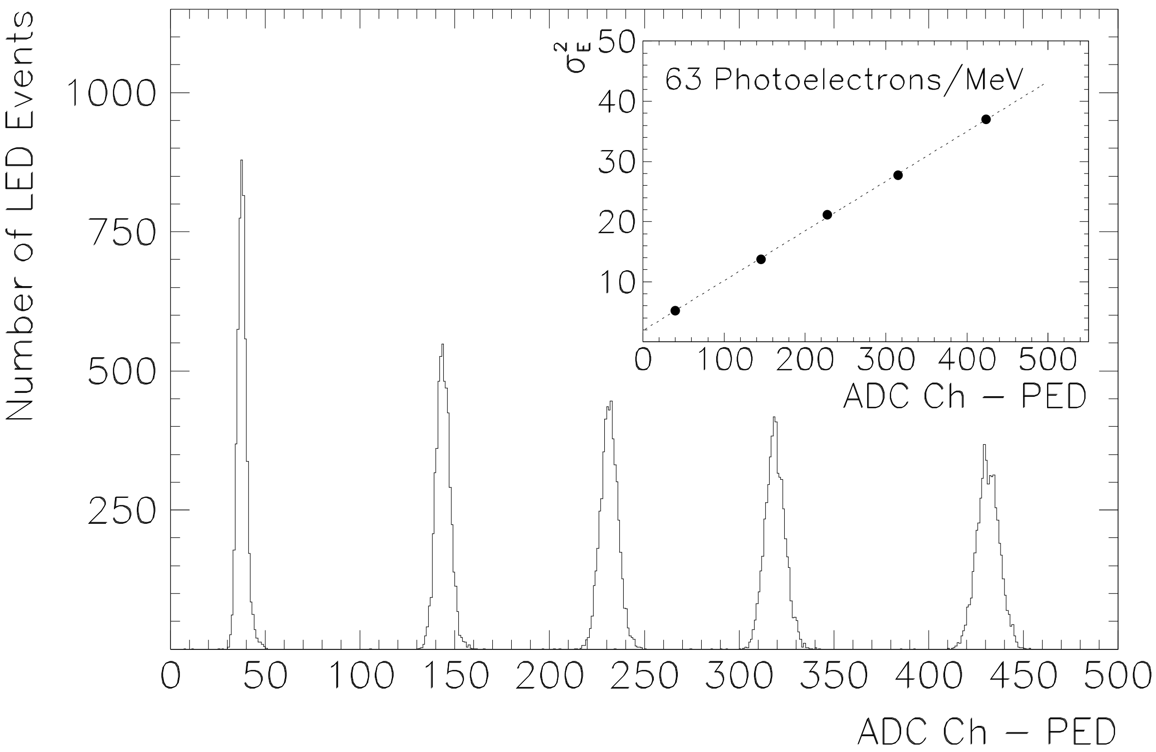
Number of LED Events
1000
750
500
250
0
50
100
150
200
250
300
350
400
450
500
ADC Ch − PED
σ_E^2
50
40
30
20
10
63 Photoelectrons/MeV
0
100
200
300
400
500
ADC Ch − PED

FIGURE 8

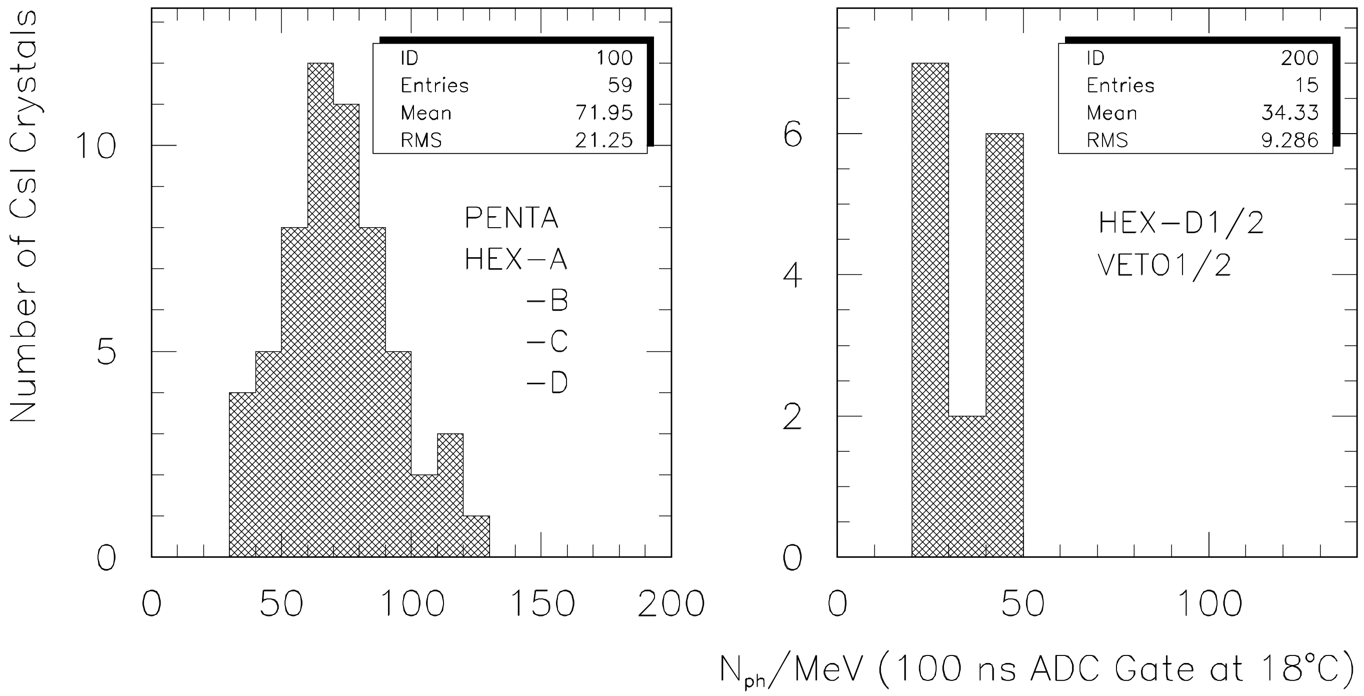
ID 100
Entries 59
Mean 71.95
RMS 21.25
PENTA
HEX−A
−B
−C
−D
Number of CsI Crystals
ID 200
Entries 15
Mean 34.33
RMS 9.286
HEX−D1/2
VETO1/2
N_ph/MeV (100 ns ADC Gate at 18°C)

FIGURE 9

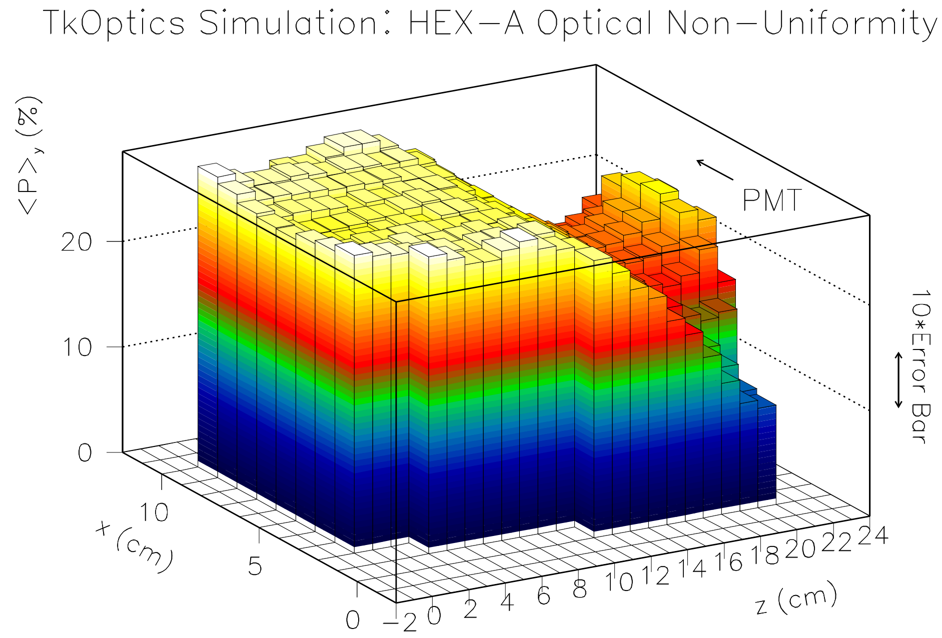

Lateral Crystal Surfaces: Specular Dielectrics r=1.00
Front Surface: Specular Dielectric r=1.00
Lateral Surface Wrapper: Diffuse Reflector r=0.90
Front Surface Wrapper: Diffuse Dielectric r=0.20
Bulk Attenuation/Scattering Length: 150 cm/200 cm

FIGURE 10

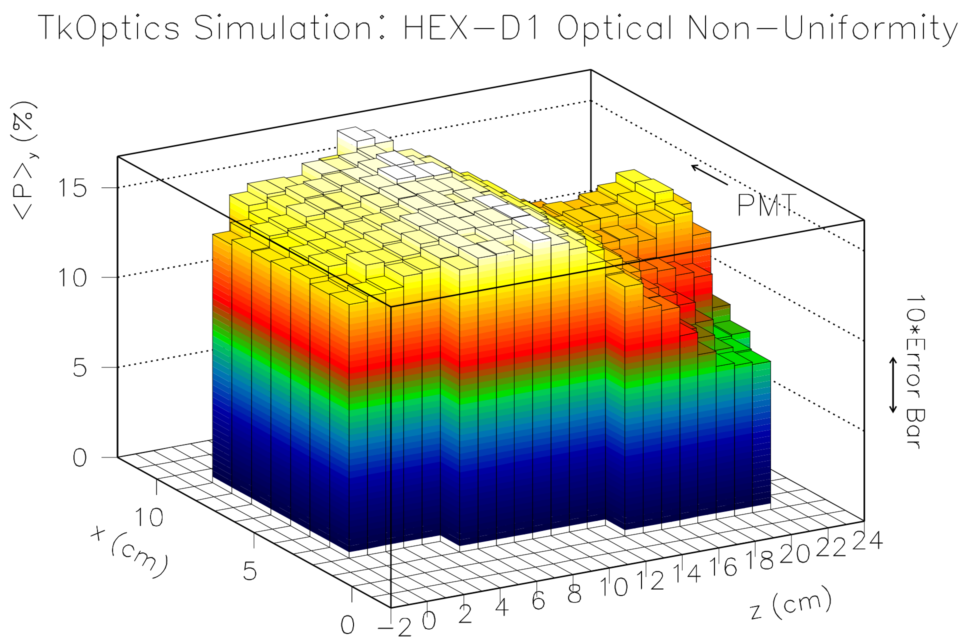

Lateral Crystal Surfaces: Specular Dielectrics r=1.00
Front Surface: Specular Dielectric r=1.00
Lateral Surface Wrapper: Diffuse Reflector r=0.90
Front Surface Wrapper: Diffuse Dielectric r=0.20
Bulk Attenuation/Scattering Length: 150 cm/200 cm

FIGURE 11

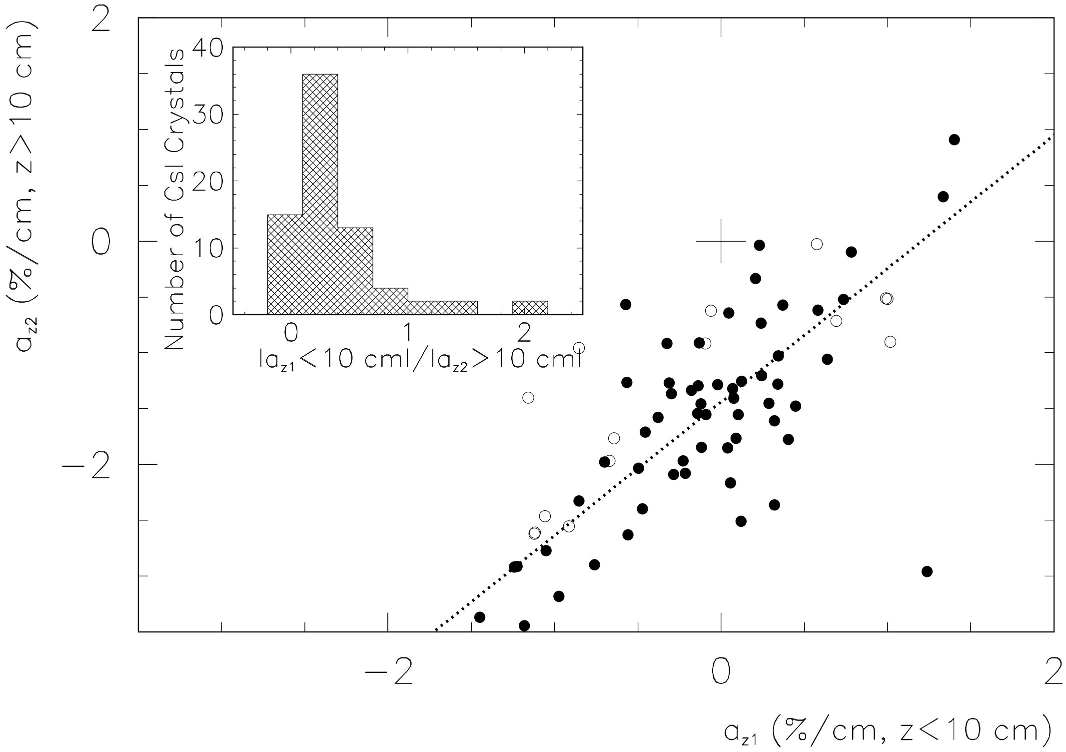

2
0
−2
−2
0
2
a_{z2} (%/cm, z>10 cm)
a_{z1} (%/cm, z<10 cm)
Number of CsI Crystals
40
30
20
10
0
0
1
2
$|a_{z1}<10 \text{ cm}|/|a_{z2}>10 \text{ cm}|$

FIGURE 12

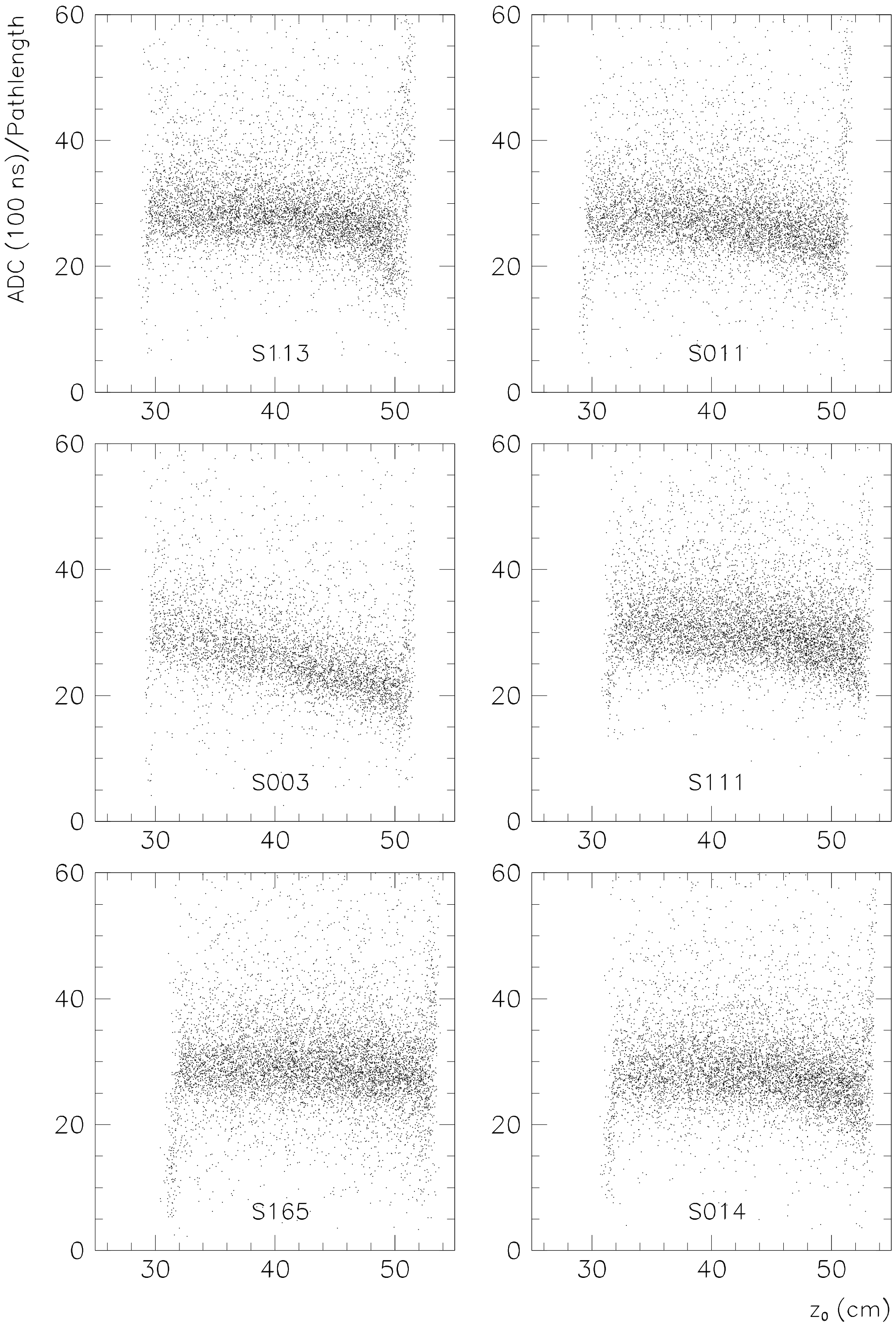
ADC (100 ns)/Pathlength
S113
S011
S003
S111
S165
S014
z_0 (cm)
0
20
40
60
30
40
50

FIGURE 13

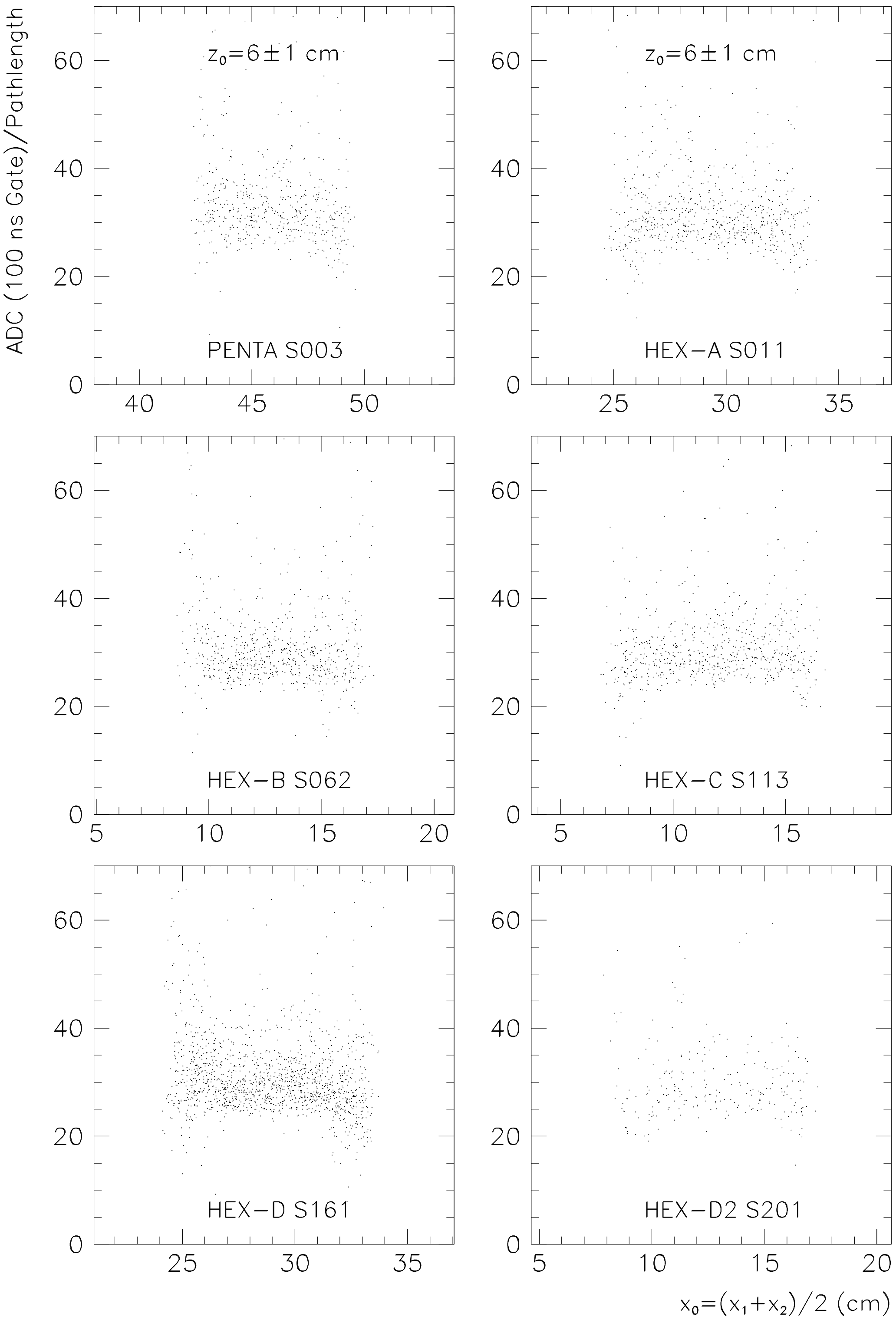
ADC (100 ns Gate)/Pathlength
z_0=6±1 cm
PENTA S003
z_0=6±1 cm
HEX−A S011
HEX−B S062
HEX−C S113
HEX−D S161
HEX−D2 S201
$x_0=(x_1+x_2)/2$ (cm)

FIGURE 14

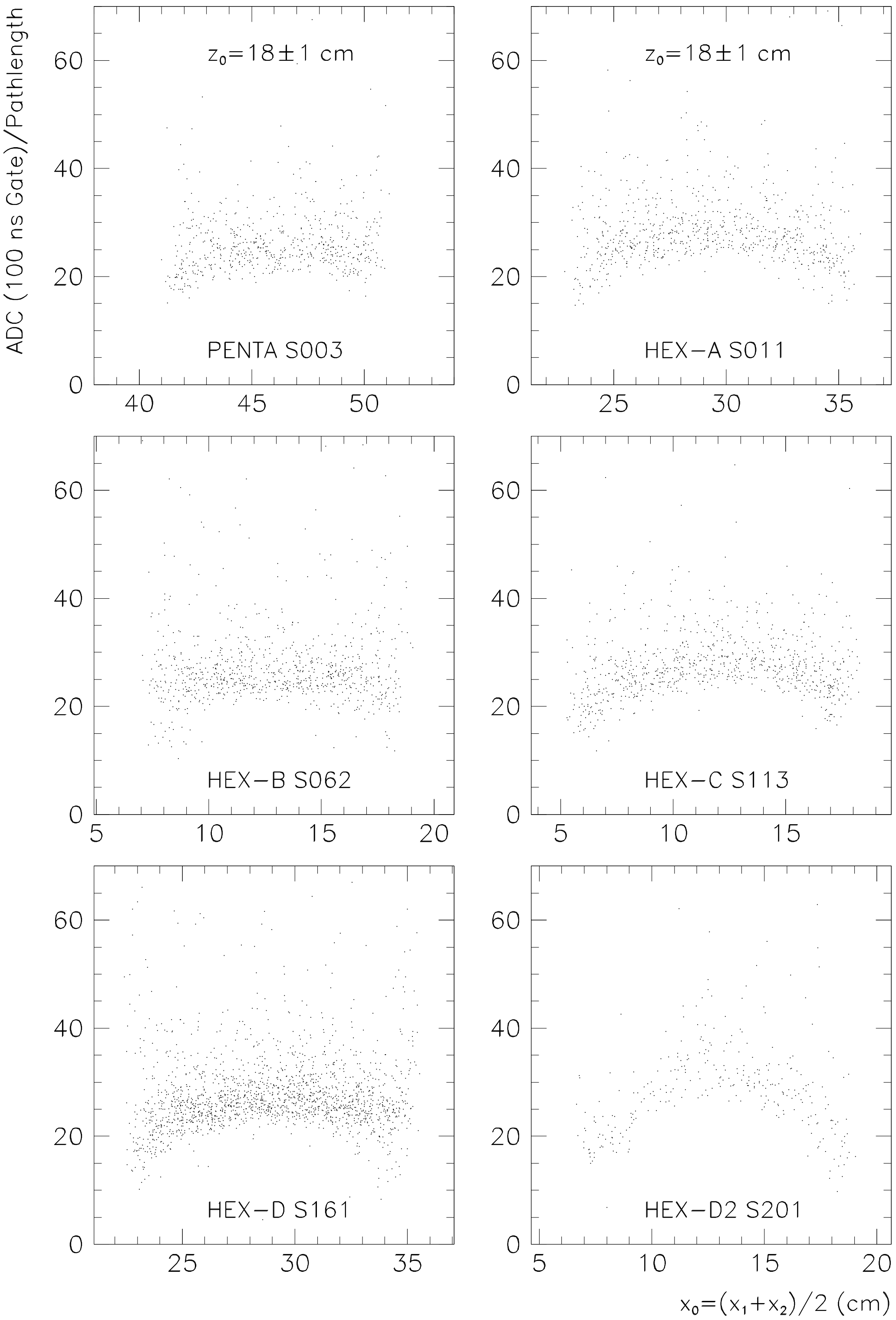
ADC (100 ns Gate)/Pathlength
z₀=18±1 cm
z₀=18±1 cm
PENTA S003
HEX-A S011
HEX-B S062
HEX-C S113
HEX-D S161
HEX-D2 S201
x₀=(x₁+x₂)/2 (cm)

FIGURE 15

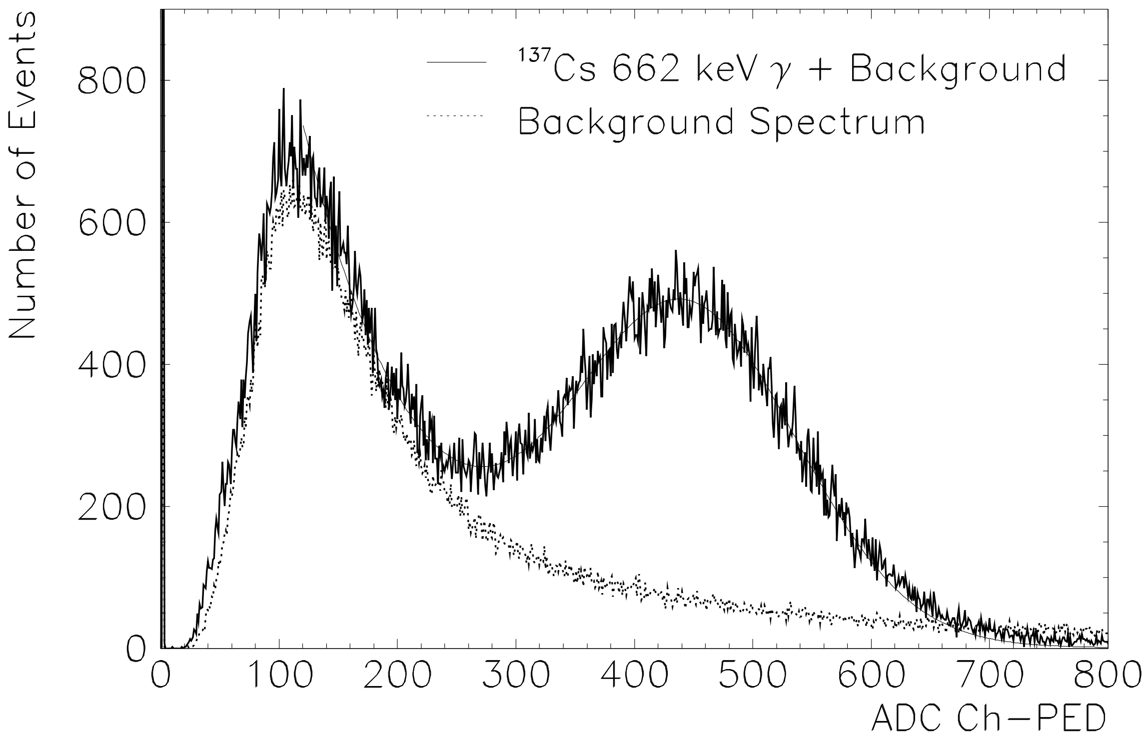
Number of Events
800
600
400
200
0
0
100
200
300
400
500
600
700
800
ADC Ch−PED
^{137}Cs 662 keV γ + Background
Background Spectrum

FIGURE 16

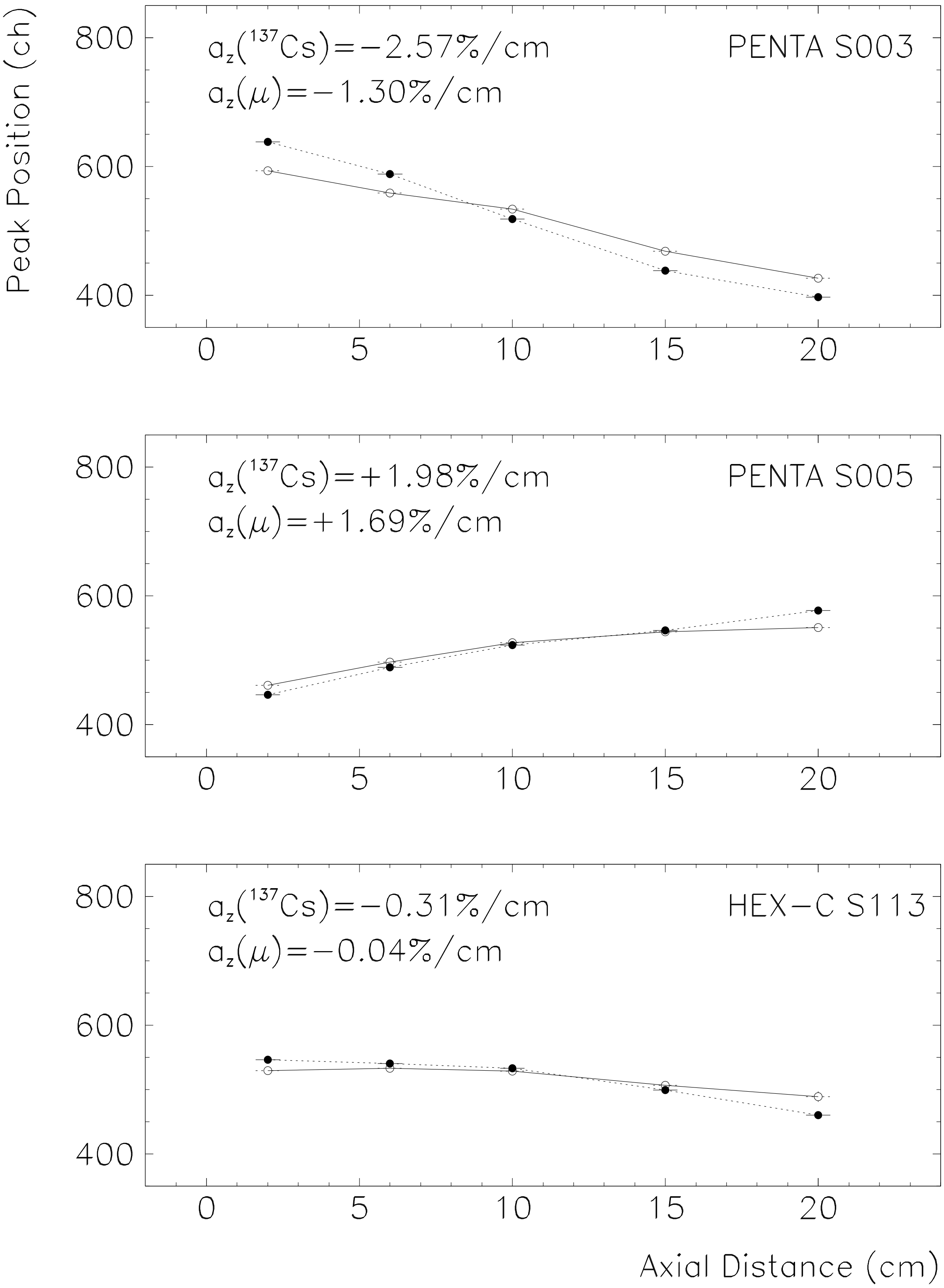
Peak Position (ch)
$a_z(^{137}Cs)=-2.57\%/cm$
$a_z(\mu)=-1.30\%/cm$
PENTA S003
$a_z(^{137}Cs)=+1.98\%/cm$
$a_z(\mu)=+1.69\%/cm$
PENTA S005
$a_z(^{137}Cs)=-0.31\%/cm$
$a_z(\mu)=-0.04\%/cm$
HEX−C S113
800
600
400
0
5
10
15
20
Axial Distance (cm)

FIGURE 17

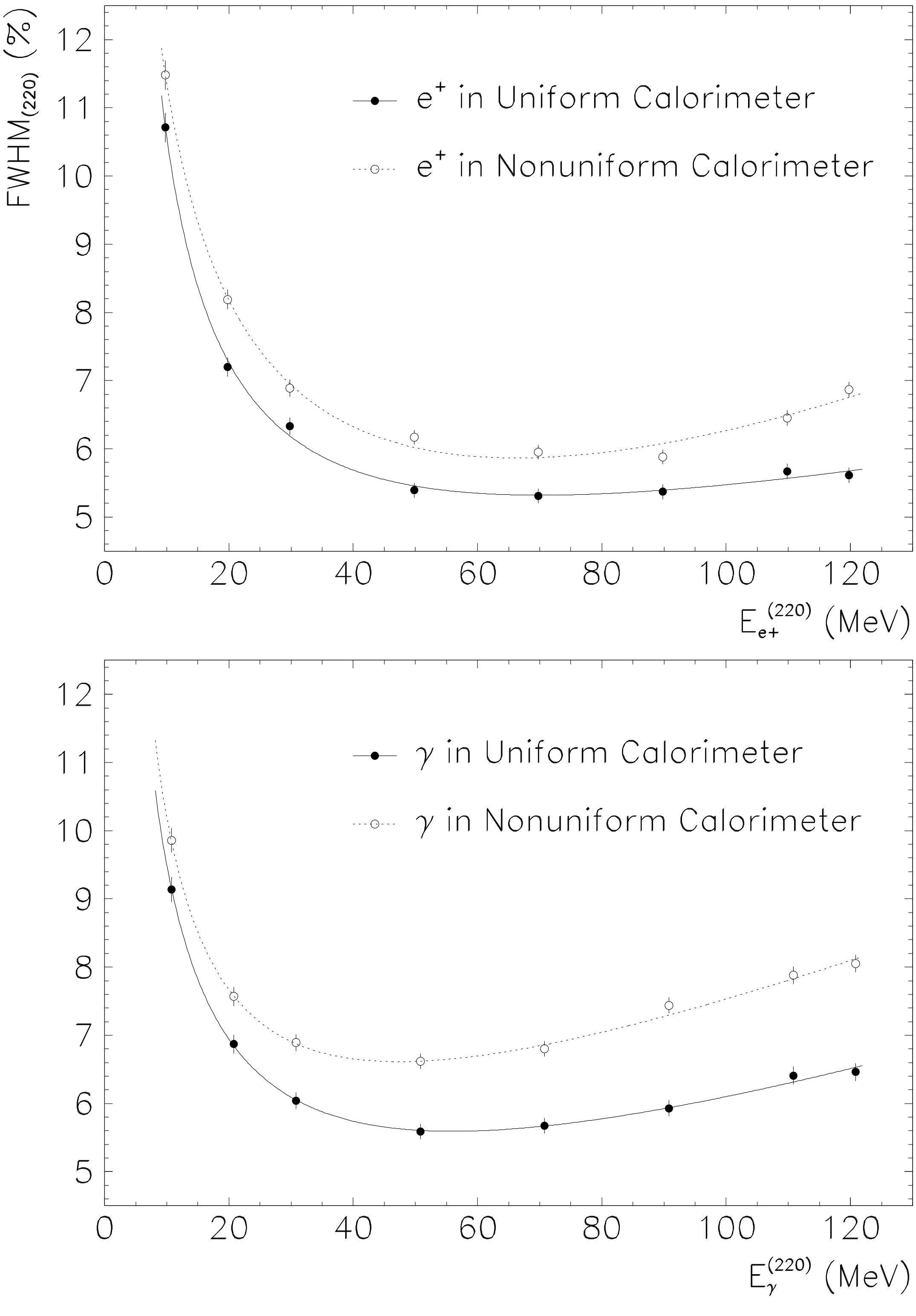

FWHM(220) (%)
e+ in Uniform Calorimeter
e+ in Nonuniform Calorimeter
E(220) e+ (MeV)
γ in Uniform Calorimeter
γ in Nonuniform Calorimeter
E(220) γ (MeV)

FIGURE 18

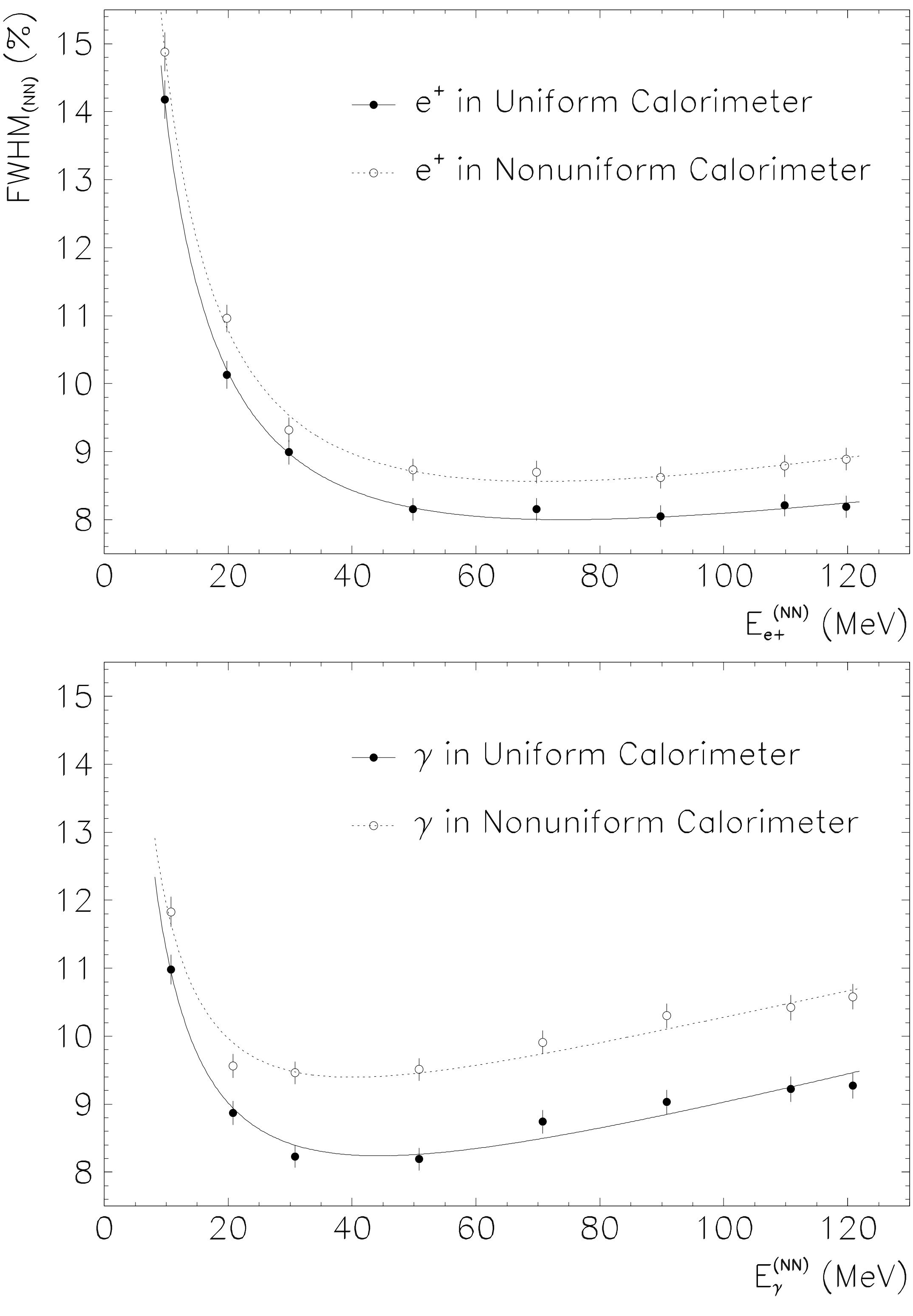
FWHM$_{(NN)}$ (%)
15
14
13
12
11
10
9
8
e$^+$ in Uniform Calorimeter
e$^+$ in Nonuniform Calorimeter
0
20
40
60
80
100
120
$E_{e+}^{(NN)}$ (MeV)
15
14
13
12
11
10
9
8
γ in Uniform Calorimeter
γ in Nonuniform Calorimeter
0
20
40
60
80
100
120
$E_{\gamma}^{(NN)}$ (MeV)

FIGURE 19

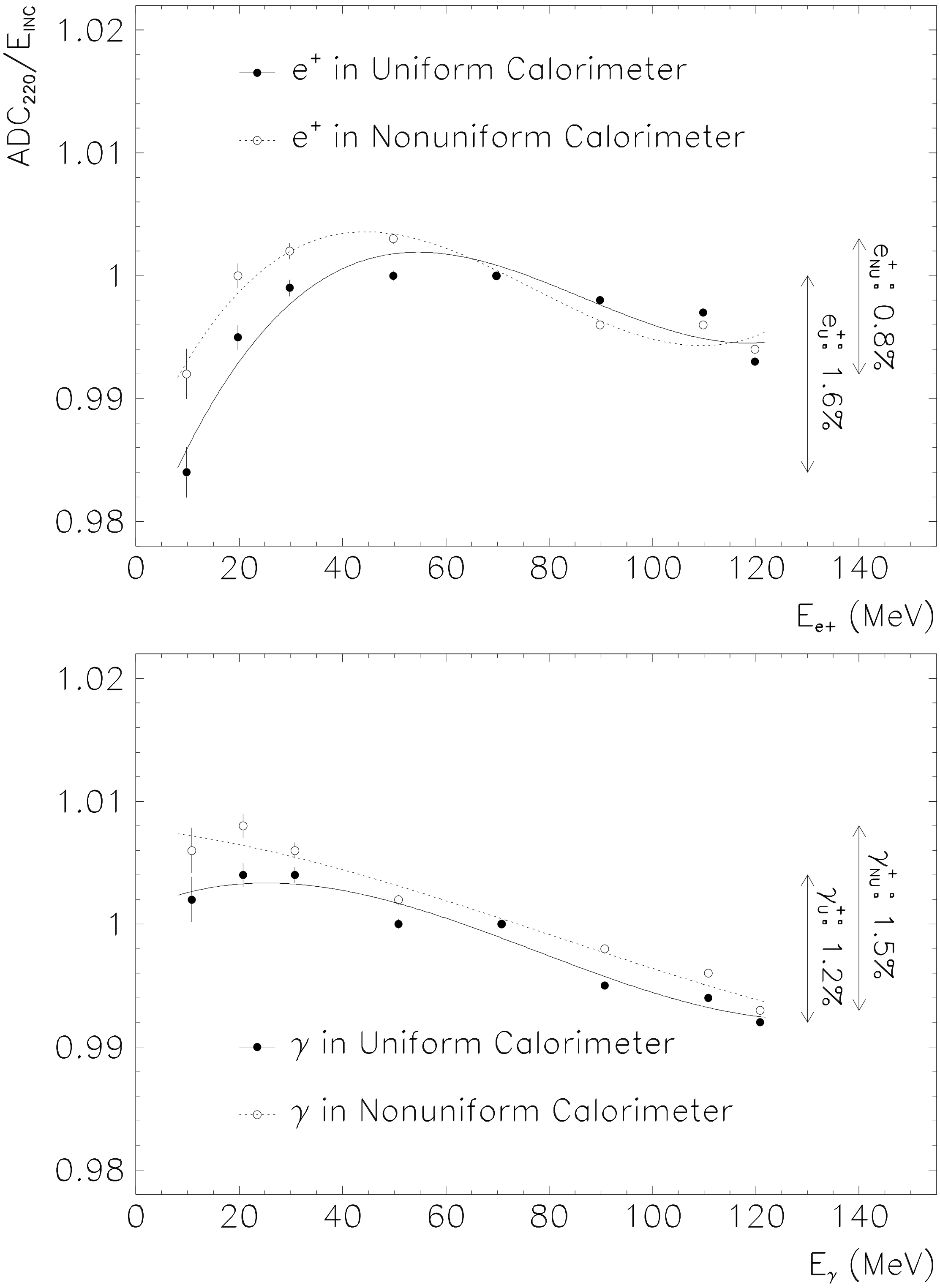

ADC$_{220}$/E$_{INC}$
e$^+$ in Uniform Calorimeter
e$^+$ in Nonuniform Calorimeter
e$^+_{NU}$: 0.8%
e$^+_{U}$: 1.6%
E$_{e+}$ (MeV)
γ in Uniform Calorimeter
γ in Nonuniform Calorimeter
γ^+_{NU}: 1.5%
γ^+_{U}: 1.2%
E$_\gamma$ (MeV)

FIGURE 20

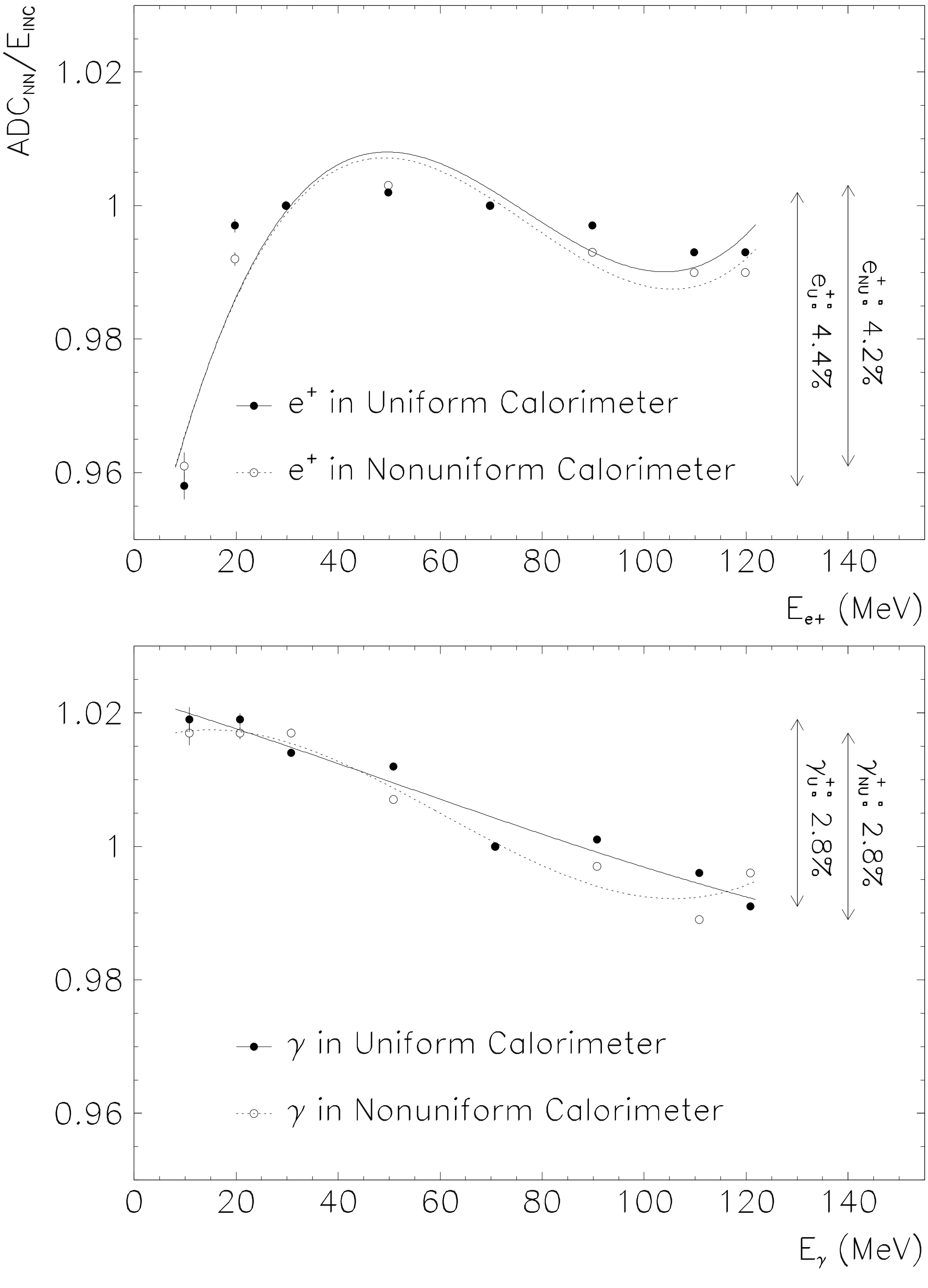
ADC_NN/E_INC
1.02
1
0.98
0.96
0
20
40
60
80
100
120
140
E_e+ (MeV)
e+ in Uniform Calorimeter
e+ in Nonuniform Calorimeter
e+_U: 4.4%
e+_NU: 4.2%
γ in Uniform Calorimeter
γ in Nonuniform Calorimeter
γ+_U: 2.8%
γ+_NU: 2.8%
E_γ (MeV)

FIGURE 21

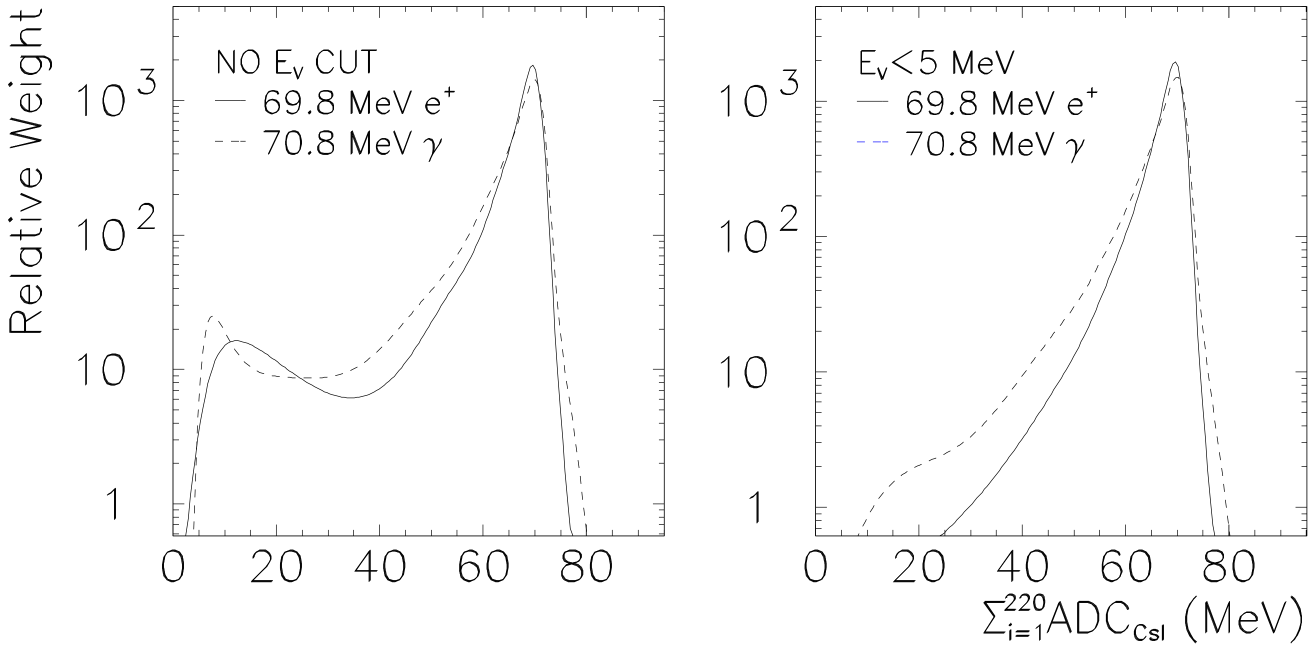

Relative Weight
NO E_v CUT
69.8 MeV e^+
70.8 MeV γ
E_v<5 MeV
69.8 MeV e^+
70.8 MeV γ
10^3
10^2
10
1
0 20 40 60 80
$\sum_{i=1}^{220} ADC_{CsI}$ (MeV)

FIGURE 22

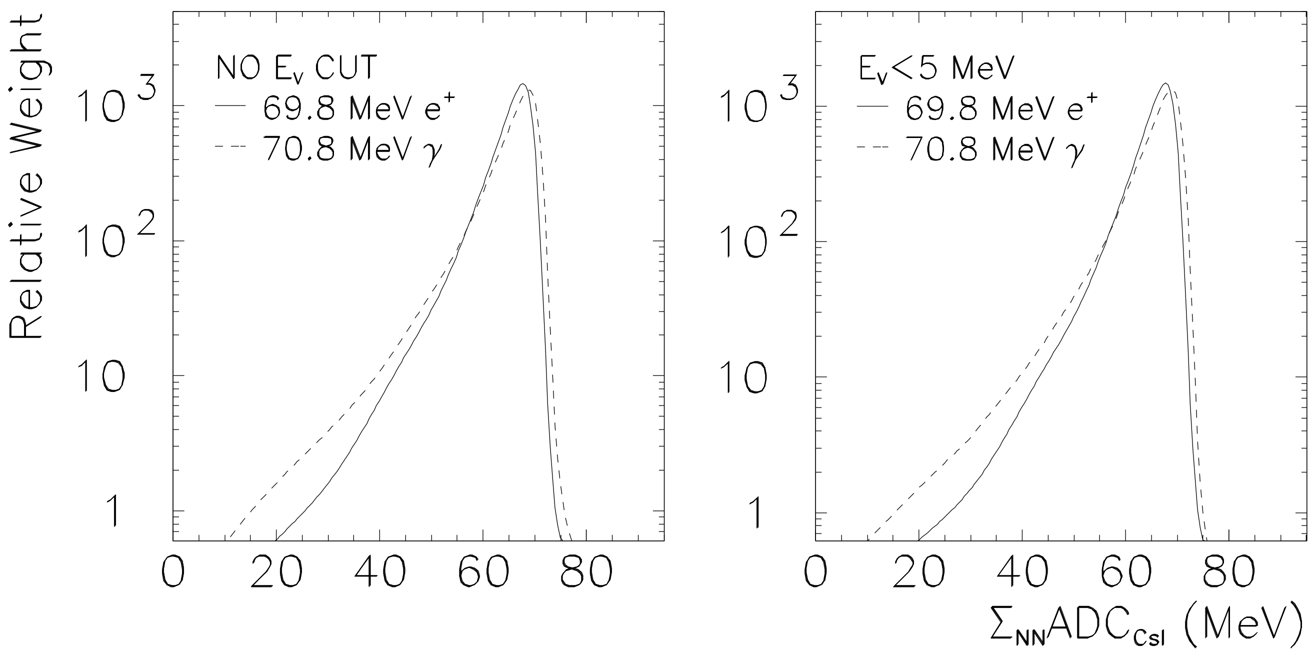
Relative Weight
NO E_v CUT
69.8 MeV e^+
70.8 MeV γ
E_v<5 MeV
69.8 MeV e^+
70.8 MeV γ
$\Sigma_{NN}ADC_{CsI}$ (MeV)

FIGURE 23